Prolonged high-grade metamorphism of supracrustal gneisses from Mühlig-Hofmannfjella, central Dronning Maud Land (East Antarctica)

Synnøve Elvevold[1*], Ane K. Engvik[2], Tamer S. Abu-Alam[1,3], Per Inge Myhre[1] and Fernando Corfu[4]

[1]*Norwegian Polar Institute, Fram Centre, P.O.Box 6606 Langnes, N-9296 Tromsø, Norway (email: elvevold@npolar.no)*

[2]*Geological Survey of Norway, P.O.Box 6315 Torgard, N-7491 Trondheim, Norway*

[3]*Currently at: The University of Tromsø - The Arctic University of Norway. P.O.Box 6050 Langnes, N-9037 Tromsø, Norway*

[4]*Department of Geosciences, University of Oslo, P.O.Box 1047 Blindern, N-0316 Oslo, Norway*

*Corresponding author

Highlights

- Gneisses from Dronning Maud Land record a prolonged Pan-African evolution characterized by ITD followed by IBC path
- Reaction textures and phase relationships in anatectic paragneisses permit a fine-scale analyses of the metamorphic evolution
- U-Pb ID TIMS geochronology on zircon and monazite are presented

Abstract

The bedrock of Mühlig-Hofmannfjella, central Dronning Maud Land in eastern Antarctica, is part of the high-grade Maud Belt and comprises a deep-seated metamorphic-plutonic complex. The *P-T-t* evolution of anatectic supracrustal gneisses has been recovered through a study of mineral assemblages, textural relationships and U-Pb ID TIMS geochronology on zircon and monazite followed by pseudosection modelling. Peak conditions reached granulite facies conditions (T ≥ 810-820°C) at moderate crustal depths (P=ca. 8 kbar) and resulted in partial melting. Peak-pressure conditions were followed by isothermal decompression at elevated temperatures. After exhumation to crustal levels of about 4-5 kbar, the area underwent a final near-isobaric cooling, which is documented by a secondary growth of garnet. Zircons indicate a period of growth at 570-566 Ma, whereas monazite ages range from 610-525 Ma. A likely heat source for the granulite facies metamorphism is decay of radioactive heat-producing elements in the core of the orogen. The combined geochronology and metamorphic data indicate a prolonged, clockwise *P-T* path, which reflects collision and formation of a long-lived orogenic plateau.

Keywords: Dronning Maud Land, Antarctica, East African/Antarctic Orogen, *P-T* path, prolonged metamorphism, hot orogen

1. Introduction

The mountain range of Dronning Maud Land (DML), East Antarctica (Fig. 1), represents a deeply eroded section through the late Neoproterozoic/Early Paleozoic East African/Antarctic Orogen (EAAO) (Jacobs et al. 1998). Metamorphic studies combined with geochronology has shown that the central part of DML has a prolonged Ediacaran-Cambrian tectonothermal history with high-grade metamorphism and granitoid magmatism that span from ca. 650 to 500 Ma. For instance, granulite facies and UHT metamorphism at 660-630 Ma has been reported from the coastal exposures of Schirmacheroasen (Henjes-Kunst, 2004; Ravikant et al., 2007; Baba et al., 2010), whereas high-grade metamorphism in the inland nunataks of the mountain belt range from 630 to 500 Ma (Jacobs et al., 2003a; Paulsson and Austrheim, 2003; Board et al., 2005; Bisnath et al., 2006, Baba et al., 2015; Pauly et al., 2016). The metamorphic complex was intruded by A-type granitoid rocks around 540-490 Ma. The granitoids are generally undeformed and include rocks of granitic, charnockitic, syenitic and monzodioritic compositions.

The apparent long and complex tectonothermal history has been interpreted in different ways. In a study by Baba et al. (2015), metamorphic zircon ages of ca. 600 and 525 Ma were obtained from pelitic, cordierite-bearing paragneisses from two different localities in central DML; Filchnerfjella and Hochlinfjellet, respectively. In both cases, the zircon ages were interpreted to represent periods immediately succeeding high-temperature peak metamorphism. The age gap of ~80 Myr was interpreted to indicate different collisional events related to separate metamorphic terranes (Baba et al., 2015).

Jacobs et al. (2003b, 2008), on the other hand, proposed a model for DML which involves a two-stage evolution; an early collision phase between 590 and 560 Ma, followed by extension, high-temperature metamorphism, tectonic exhumation and emplacement of intrusive rocks around 530-490 Ma. The early compressional stage resulted in the major, strong deformation and medium- to high-grade metamorphism and growth of metamorphic zircon rims on older cores (Jacobs et al. 2003b). The extensional stage resulted in isothermal decompression, high-grade reworking (Engvik and Elvevold, 2004) and is characterized by metamorphic as well as magmatic zircon growth (Jacobs et al. 2008).

Geological work in Dronning Maud Land is still fragmentary, available metamorphic age data from the central part of the mountain range are scattered and the *P-T-t* paths are not well constrained. In this contribution, we present new high-precision U-Pb ID TIMS data from zircons and monazite from high-grade supracrustal rocks in Mühlig-Hofmannfjella. Large parts of the thermal history are preserved within zircon and monazite populations in individual samples. We focus on integrating metamorphic petrology, pseudosection modelling and U-Pb geochronology, use the data to infer a *P-T-t* path of area, and add to the data and discussions provided by previous studies.

2. Geological background

The East African/Antarctic Orogen (EAAO) is one of the largest orogen on Earth and formed during multi-plate collision of various parts of East and West Gondwana (e.g. Stern, 1994; Kröner and Stern, 2005; Fritz et al., 2013). Dronning Maud Land is interpreted to represent the southernmost segment of EAAO (e.g. Jacobs et al. 1998; 2003b; Grantham et al., 2011), although this view has been challenged by Collins and Pisarevsky (2005).

The Maud Belt in western and central DML comprises a metamorphic complex that stretches from Heimefrontfjella in the west through Kirwanveggen, H.U. Sverdrupfjella, Gjelsvikfjella, and Mühlig-Hofmannfjella eastwards (Fig. 1). Previous work has shown that the mountain range has a complex tectonothermal history, which involves two main tectonothermal events; the first in late Mesoproterozoic and the second in Ediacaran-Cambrian times (e.g. Jacobs et al., 1998, 2003a; Paulsson and Austrheim, 2003; Bisnath et al., 2006; Grosch et al. 2015). Outcrop scale structures, as well as mineral assemblages, related to the Mesoproterozoic metamorphic event are difficult to recognize because of the strong Ediacaran-Cambrian overprint. The Mesoproterozoic tectonothermal event is related to the assembly of Rodenia, whereas the younger event is related to the assembly of Gondwana. The Ediacaran-Cambrian event is commonly referred to as the Pan-African orogeny (Kennedy, 1964). The metamorphic rocks in central DML display a strong, high-grade Pan-African overprint, although late Mesoproterozoic protolith ages, as well as metamorphic ages, between 1.2-1.0 Ga are reported (Jacobs et al., 1998, 2003a; Paulsson and Austrheim, 2003; Bisnath et al., 2006).

The bedrock of western and central DML comprises a metamorphic-plutonic complex where the metamorphic sequence includes gneisses and migmatites of various compositions, which typically contain granulite- or upper amphibolite facies mineralogy. The metamorphic rocks are intruded by an igneous suite, which includes voluminous masses of granite, charnockite, quartz-syenite, monzonite, monzodiorite and several generations of dykes. Some of the granitoids are characterized by Fe-enriched bulk composition and contain fayalite (Ohta et al., 1990). The intrusions show distinctive within-plate geochemistry (D'Souza et al. 2006). The early Ediacaran-Cambrian intrusions show various degrees of deformation (Mikhalsky et al., 1997; Jacobs et al., 1998), while the later quartz-syenites are mainly undeformed, except for late shear zones and brittle faults. The igneous rocks in central DML intruded between 540 and 500 Ma (Mikhalsky et al., 1997; Paulsson and Austrheim, 2003; Jacobs et al., 2003b; Markl and Henjes-Kunst, 2004; Jacobs et al., 2008).

Spectacular examples of fluid-rock interaction phenomena are widespread in central DML (Markl and Piazolo, 1998; Ohta, 1999; Engvik et al., 2005). The fluid-rock interactions form discordant light bands with a central pegmatite or aplite vein (Engvik et al., 2005, 2009; Bucher and Frost, 2005; Engvik and Stöckhert, 2007), and were formed by infiltrating of H_2O-CO_2 volatiles into the characteristic brownish high-grade granitoids. The late pegmatites, fluid infiltration and associated alteration in a quartz-syenite in Filchnerfjella was dated to around 486 Ma by U-Pb ID-TIMS dating of titanite (Paulsson, 2003). Cooling during the latest stage of the orogeny has been recorded by $^{40}Ar/^{39}Ar$ hornblende-, biotite- and K-feldspar ages, which range from ca. 480 to 435 Ma (Hendriks et al., 2013).

3. Analytical methods

The investigated samples from Mühlig-Hofmannfjella were collected during the Norwegian Antarctic Research Expedition 1996/97 (NARE 96/97). Detailed petrographic studies were performed by optical microscopy and scanning electron microscopy (SEM) using a LEO1450 VP instrument at the Geological Survey of Norway (NGU), including mineral identification with an energy-dispersive spectrometer (EDS) mounted on the SEM. Quantitative microanalyses of mineral phases (Tables 1-4) were obtained using a Cameca SX100 electron microprobe equipped with five wavelength-dispersive spectrometers at the Institute of Geosciences, University of Oslo. The accelerating voltage was 15 kV and the counting time 10 s on peak using a beam current of 15 nA. Natural and synthetic silicate and oxides standards were used for calibration. Data reduction was done with the PAP program (Pouchou and Pichoir, 1984). Mineral abbreviations are after Whitney and Evans (2010). The chemical formula were calculated using AX program (https://www.esc.cam.ac.uk/research/research-groups/research-projects/tim-hollands-software-pages/ax). The following assumptions are used to calculate Fe^{2+}/Fe^{3+} ratio: for garnet - total cations are 8 for 12 oxygens; for biotite – the summation of tetrahedral and octahedral cations is 6.9 for 11 oxygens; for cordierite - total cations are 11 for 18 oxygens; for plagioclase – all the iron is ferric oxide.

The bulk rock compositions were analyzed at NGU, measured on fused glass beads prepared by 1:7 dilution with lithiumtetraborate. The samples were analyzed on a PANalytical Axios XRF spectrometer equipped with a 4 kW Rh X-ray end-window tube, using common international standards for calibration.

The U-Pb analyses on zircon and monazite (Table 5) were carried out by ID-TIMS (Krogh, 1973) at the University of Oslo. The selected zircons were subjected to chemical abrasion by annealing at 900 ^{o}C and partial dissolution overnight in concentrated HF at about 190 ^{o}C (adapted from Mattinson, 2005). Monazite was analyzed without abrasion. The U-Pb analyses were done using a mixed ^{202}Pb-^{205}Pb-^{235}U tracer. The blank correction was ≤2 pg for Pb and 0.1 pg for U. A more detailed description of the procedure in the Oslo laboratory is given in Corfu (2004). The decay constants are those of Jaffey et al. (1971). The data were calculated and plotted using the program Isoplot (Ludwig 2009).

4. Field relations

The mountains and nunataks of Mühlig-Hofmannfjella (3ºE30'E to 7ºE and 71º40'S to 72º10'S) are situated in central DML (Fig. 1) and belong to the Maud Belt. The northern part of Hochlinfjellet (Figs. 1c, 2a), consists of supracrustals, grey gneisses and migmatites. The strongly deformed supracrustal sequence, comprising calc-silicate rocks, garnet-biotite gneiss, garnet-sillimanite-cordierite gneiss and migmatites, is intruded by monzonite and charnockite

(Fig. 2b). The pelitic garnet-bearing gneisses are weakly to strongly foliated, fine- to medium-grained and display a characteristic brownish weathering color (Figs. 2c, d). The migmatitic gneisses appear as metatexite, diatexite and raft migmatite. The descriptions below focus on selected samples of garnet-sillimanite-cordierite gneiss and garnet-biotite gneiss.

5. Petrography and mineral chemistry

5.1 Garnet-sillimanite-cordierite gneiss (AHA240, AHA242, AHA245)

The gneisses contain variable portions of garnet, sillimanite, cordierite, quartz, feldspar and minor biotite. The feldspars are plagioclase, microcline, perthite and minor antiperthite. Accessory minerals are spinel, ilmenite, magnetite, graphite, monazite and zircon. The microtexture is characterized by an inequigranular matrix of quartz, feldspars and cordierite. The matrix minerals define a slight grain flattening fabric and display highly irregular and lobate grain boundaries. The grainsize of matrix quartz and feldspar varies between 0.2 – 4 mm. Quartz form coarse, flattened grains, up to 3 mm long, and commonly includes tiny biotite laths and plagioclase.

Garnet occurs in two textural varieties; i) as anhedral, poikiloblastic grains Grt_1, up to 8 mm, and ii) as small euhedral to subhedral grains Grt_2, 0.2 to 1 mm (Fig. 3a). Grt_1 includes quartz, biotite and ilmenite, and is frequently surrounded by a cordierite moat. The smaller Grt_2 grains are often clustered in elongated biotite-rich aggregates parallel to the foliation or as small grains in cordierite-rich domains. Grt_2 include quartz and more rarely fibrolitic sillimanite or cordierite (Fig. 3b).

Core compositions of Grt_1 in sample AHA245 are almandine (X_{alm} = 0.79-0.80) with pyrope (X_{prp} = 0.16-0.17) and minor grossular (X_{grs} = 0.03-0.04) and spessartine (X_{sps} = 0.01). Grt_1 is weakly zoned with increasing almandine (by 0.01-0.02 units) and decreasing pyrope (by 0.01-0.02 units) towards the rim, whereas the grossular and spessartine content is homogenous. The Fe/(Fe+Mg) values show a rimward increase from 0.83 to 0.85, and this zoning pattern is interpreted as a retrograde feature.

Grt_2 is slightly more almandine-rich than the larger Grt_1. Core composition of Grt_2 is X_{alm} =0.81-0.82, X_{prp}=0.13-14, X_{grs}<0.035 and X_{sps}<0.02. Compositional zoning is present along the crystal rims and is characterized by a rimward increase in Fe and Fe/(Fe+Mg) (Fe and Mg show antithetic patterns). Rim composition is X_{alm} =0.83-0.85, X_{prp}=0.10-12, X_{grs}<0.035 and X_{sps}<0.02.

Two generations of *sillimanite* are present. Primary sillimanite, Sil_1, occurs as scattered euhedral crystals in the matrix, and as inclusions in cordierite. A later generation of sillimanite (Sil_2) appears as secondary overgrowth on Sil_1 (Fig. 3c) and as fibrolite along grain boundaries of matrix minerals.

Cordierite is present as i) inclusions in Grt_2 (Fig. 3b) and ii) as unaltered, equidimensional grains in the matrix. It commonly surrounds and encloses spinel and sillimanite (Fig. 3d), and more rarely biotite. Small inclusions of zircon and monazite are surrounded by pleochroic haloes. Matrix cordierite is unzoned with X_{Fe} =0.41. Microprobe analyses are in the range 98-99 wt% indicating the presence of CO_2, H_2O, N_2 or other gases.

Feldspar is present as plagioclase, K-feldspar and as minor perthite and antiperthite. Cuspate habit and low dihedral angles of feldspar grains suggest late crystallization of partial melts (Fig. 3e). Plagioclase cores are An_{35-36} whereas partly recrystallized rims are An_{25-26}. Antiperthite has the composition An_{36} and Or_{88}. Non-perthitic K-feldspar is Or_{86-88}, whereas perthitic alkali feldspar has the composition Or_{85}.

Minor *biotite* forms small, lath-like crystals with a distinct reddish-brown color, coexisting with garnet (Grt_2) and matrix minerals (Fig. 3a). Biotite also occurs as rounded inclusions within K-feldspar, quartz, garnet and cordierite. Very fine-grained biotite + quartz symplectites are observed in contact with garnet (Fig. 4a). Matrix biotite is commonly associated with graphite rods. The mineral chemistry of biotite is closely related to its textural appearance. Core composition of matrix biotite and biotite included in K-feldspar has the highest Fe/(Fe+Mg) ratio, which is in the range 0.63-0.65. Biotite included in garnet generally has lower values (0.42-0.53) of Fe/(Fe+Mg) than matrix biotite. The highest Ti-contents (up to 6.5 wt %) are analyzed in biotite included in K-feldspar and garnet.

Spinel is present as clusters of green and brown grains included in cordierite (Fig. 3d), plagioclase and sillimanite. It is not observed in contact with quartz or any other matrix minerals. Spinel is hercynite with X_{Fe}=0.72-0.74 and X_{Zn}=0.10-0.19.

5.2 Garnet-biotite gneiss (AHA241, AHA244)

The garnet-biotite gneiss is fine-grained, strongly foliated and contains a higher proportion of biotite than the garnet-sillimanite-cordierite gneiss. The fabric is defined by oriented interstitial biotite, elongated clusters of garnet and flattened quartz grains. Major minerals are garnet, plagioclase, K-feldspar, quartz and biotite, and accessory minerals are orthopyroxene, apatite, ilmenite, graphite, zircon and monazite. The grain size of the quartz-feldspar matrix is 0.1-0.5 mm, larger flattened quartz grains are up to 2 mm long. Unlike the garnet-sillimanite-cordierite gneiss, the garnet-biotite gneiss shows no textural evidence for more than one generation of garnet, however, the core region of the larger garnets might belong to an older generation. Subhedral to euhedral garnet porphyroblasts (Grt_1?/Grt_2) are 0.2-4 mm and include abundant quartz (Fig. 3f) and minor orthopyroxene (Opx_1). Garnets show straight grain boundaries with biotite (Fig. 4b). Matrix biotite (Bt_2) is commonly associated with graphite rods. Quartz includes small rounded biotite laths.

The core composition of *garnet* (Grt_1?/Grt_2) is almandine (X_{alm} = 0.68-0.69) with pyrope (X_{prp} = 0.23-0.24) and minor grossular (X_{grs} = 0.05-0.06) and spessartine (X_{sps} = 0.02-0.03). The Fe/(Fe+Mg) ratio for core is in the range of 0.74-0.75. The rim composition (Grt_2) is X_{alm} =0.69-0.70, X_{prp}=0.22, X_{grs}< 0.065 and X_{sps}< 0.03. The values of the Fe/(Fe+Mg) ratio of garnet rim is 0.75-0.76, whereas the values are 0.82-0.83 when in contact with matrix biotite.

Fe/(Fe+Mg) values of *biotite* ($Bt_{1?/2}$) included in garnet are in the range 0.22-0.30, whereas values for matrix biotite (Bt_2) are around 0.38. Ti values of biotite are in the range 0.21 to 0.32 a.p.f.u.

Orthopyroxene (Opx_1) is present as small inclusions in garnet. Analyzed orthopyroxene has the composition En_{58-63}, and the maximum Al_2O_3 content is 1.99 wt%.

Core composition of matrix *plagioclase* (Pl_2) is $An_{47-51}Ab_{39-52}Kfs_{0-0.01}$, whereas analyses of plagioclase ($Pl_{1?}$) included in garnet is $An_{47}Ab_{53}$.

5.3 Textural interpretation

The early peak assemblages in the garnet-sillimanite-cordierite gneiss are interpreted to comprise Grt_1 + Sil_1 ± Spl + Ilm + Qtz ± Bt + ternary feldspars (perthite and antiperthite) + melt, which are indicative of granulite facies conditions. Garnets that occur in leucocratic layers are interpreted to be peritectic products formed during biotite dehydration melting. The presence of ternary feldspars is further indication of high-temperature granulite facies metamorphism. The peak assemblages are partially overprinted by cordierite-bearing assemblages. Grt_1 is surrounded by a cordierite moat (Fig. 3a), while larger cordierite crystals commonly include sillimanite + spinel + ilmenite aggregates. These textures, which are frequently observed in pelitic granulites, are typically formed during decompression at elevated temperatures. Similar textures have been described by Elvevold and Engvik (2013) in equivalent gneisses from Filcherfjella, ca. 100 km east of Hochlinfjellet.

A second-generation garnet, Grt$_2$, is found in garnet-sillimanite-cordierite gneiss, and is present as small, subhedral to anhedral grains. Grt$_2$ enclose fibrolitic sillimanite (Sil$_2$) and cordierite (Fig. 3b) in addition to quartz. Grt$_2$ may also occur as overgrowth on older garnet (Grt$_1$), although this is not easily detected. Grt$_2$ is in equilibrium with matrix biotite, which is interpreted to have formed during retrograde evolution of the gneisses, together with secondary fibrolitic sillimanite (Sil$_2$) (Fig. 3c). There are no unequivocal textures indicating to which degree feldspars recrystallized during post-peak conditions.

Whereas the garnet-sillimanite-cordierite gneisses comprise relict granulite facies assemblages, the matrix minerals in garnet-biotite gneiss is interpreted to represent a retrograde amphibolite facies assemblage. Subhedral to euhedral garnets, which coexist with matrix biotite, are interpreted to be secondary with respect to the peak assemblage. The peak metamorphic assemblage in the garnet-biotite gneiss is interpreted to comprise a garnet + orthopyroxene-bearing granulite facies assemblage. Orthopyroxene is only present as tiny inclusions in garnet and was most probably removed from the equilibrium assemblage during retrogression. As some of the garnet porphyroblasts are large (i.e. 4 mm), the cores regions of theses garnet might be part of the peak assemblage. Phase equilibria modelling, see below, demonstrates that prograde garnet was, at least partly (i.e. rims), consumed during decompression before it resumed growth on isobaric cooling.

6. Phase equilibria modelling

Pseudosections, which illustrate the stability fields of different equilibrium mineral assemblages for a given bulk rock composition, have been calculated for two different bulk compositions using Perple_X version 6.8.6 (http://www.perplex.ethz.ch/; Connolly, 2009) and the most recent internally consistent dataset, hp62ver, of Holland and Powell (2011). The following activity-composition models were used; garnet (Holland and Powell, 1998); ternary feldspar (Fuhrman and Lindsley, 1988); biotite (White et al., 2007); orthopyroxene (Holland and Powell, 1996); melt (White et al., 2001; Holland and Powell, 2001); cordierite (White et al., 2014). The albite-in and the K-feldspar-in boundaries in all pseudosections were calculated by setting the Na/(Na+Ca+K) and K/(Na+Ca+K) of the ternary feldspar solution model to zero; respectively.

Phase diagrams were calculated for the *P*-*T* range 2-10 kbar and 550-900°C for the XRF analyses cited in the caption for Fig. 5. Sample AHA245 (garnet-sillimanite-cordierite gneiss) comprises minerals with Fe^{3+} (i.e. cordierite) and was accordingly modelled in the NCKFMASHTO system. The modelling was undertaken in the NCKFMASHT system for sample AHA244 (garnet-biotite gneiss). Iron was assumed to be Fe^{2+} as the Fe^{3+} content of the minerals considered in this sample is negligible and Fe^{3+} oxides are not present. For both samples, the Mn content is minor and is therefore not included into the system. The Ca content has been adjusted to account for the presence of apatite, which is observed in all samples. The water content during peak conditions was estimated by calculating T-M_{H2O} pseudosections at constant pressure. A near-peak pressure estimate of 8 kbar was used based on "average pressure" calculations using the program THERMOCALC (Powell and Holland, 1988, Table 6).

The pseudosections are based on the measured bulk composition of anatectic gneisses that most probably have experienced melt loss during their prograde evolution. The reintegration of melt into the measured rock composition requires knowledge of the amount of melt that was lost, which is difficult to constrain. Although the melt-reintegration approach has become an increasingly used method (Bartoli, 2017 and references therein), it is beyond the scope of this study. The calculated diagrams, using the composition of residuum after anatexis and melt extraction, are therefore only appropriate for evaluating the near-peak and early retrograde evolution of the gneisses.

Sample AHA244 shows petrographic evidence of re-equilibration during retrograde conditions. In order to model the retrograde evolution, a new effective bulk composition was calculated by removing the garnet cores (30% of the garnet chemical composition) from the measured bulk chemistry using the rbi function of the THERMOCALC.

6.1 Garnet-sillimanite-cordierite gneiss (AHA245)

The T-M_{H2O} pseudosection for the garnet-sillimanite-cordierite bearing gneiss is shown in Figure 5a. The peak assemblage Grt_1-Sil_1-Bt-ternary feldspars-Qtz melt defines a trivariant field which extend over the full range of M_{H2O} in the temperature range 740-795 ^oC. The value for the H_2O content at the peak conditions was chosen to be equivalent to the M_{H2O} at the lowest temperature where the near-peak assemblage containing melt occurs, i.e. M_{H2O} of 0.78, which is equal to 2.73 mol% of H_2O in the system.

The calculated pseudosection for sample AHA245 is shown in Fig. 6. The stability field for the assemblage Grt_1-Sil_1-Bt-Kfs-Pl-Qtz-melt is constrained by the temperature range 750-820^oC and pressures above 5 kbar (A in Fig. 6a). If we assume that biotite was absent from the peak assemblage (i.e. Grt_1-Sil_1-Kfs-Pl-Qtz-melt) the calculated pseudosection constrain the peak conditions to T > 825 ^oC and P > 7 kbar (A' in Fig. 6a). Small biotite grains are included in cordierite, which suggests that biotite was present when cordierite formed during the early stage of decompression. Biotite was most probably removed from the assemblage as the *P-T* path entered the Grt-Crd-Sil-melt field (B in Fig. 6a). Further decompression lead to continued growth of cordierite and consumption of garnet and sillimanite (C in Fig. 6a), as indicated by textural relationships.

Sample AHA245 is characterized by growth of secondary garnet (Grt_2) as well as secondary fibrolitic sillimanite (Sil_2), and textural relationships suggest that Grt_2 and Sil_2 were produced by breakdown of cordierite (Fig. 3b, c). The final melt crystallized during cooling as the *P-T* path crossed the Grt-Bt-Crd-Liq field into the Grt-Bt-Sil-Crd field around 750 ^{o}C and 4 kbar (D in Fig. 6a).

Calculated mineral isopleths for grossular in garnet (Ca/(Ca+Fe+Mg) in garnet) and anorthite in plagioclase (Ca/(Ca+Na+K) in plagioclase) are shown in Fig. 6b. Because the diffusion rate of Ca in garnet is thought to be several orders slower than that of Fe and Mg (e.g. Spear, 1993), we consider the grossular component of large garnet cores (Grt_1) to have the best potential to represent the mineral composition at the thermal peak. Likewise, because intracrystalline diffusion in plagioclase involves coupled CaAl – NaSi exchange, diffusion processes in plagioclase are limited during cooling. The measured mineral compositions of garnet core and plagioclase inclusions in garnet plot within the Grt-Sil-Bt-melt field, and the intersection of the mineral isopleths X_{Grs} and X_{An} indicate equilibration around 8 kbar and 810^{o}C (Fig. 6b). It is worth noticing that the X_{An} isopleths are widely spaced and slight variations in the plagioclase composition will have large impact on the pressure estimation.

In order to evaluate the garnet growth history of the sample, garnet modes were calculated and contoured molar quantities are plotted in Fig. 7a. The plot demonstrates that the highest garnet mode (between 10-12 vol %) is at peak conditions. With decreasing pressure, the garnet mode decreases as garnet is being consumed to form cordierite. A small amount of garnet will resume growth on isobaric cooling around the boundary between the Grt-Bt-Crd-

Sil and the Grt-Bt-Sil field (740-720°C at 4.5-5 kbar), and on further cooling from ca. 700 °C the garnet mode will slowly decrease again.

6.2 Garnet-biotite gneiss (AHA244)

The garnet-biotite gneiss is modelled in the NCKFMASHT system. The water content was estimated by calculating T-M_{H2O} pseudosection (Fig. 5b). The field containing the assumed peak assemblage Opx-Pl-Kfs-Grt-Liq-Qtz-Ilm is stable above 825°C at M_{H2O} < 0.6. If we consider the near-peak assemblage Bt-Pl-Kfs-Grt-Liq-Qtz-Ilm, we have chosen values for M_{H2O} at the lowest temperature for this assemblage (M_{H2O}=0.25), which corresponds to 1.9 mol% of H_2O in the system.

Figure 8a shows the calculated phase diagram for garnet-biotite gneiss. The high-temperature side of the phase diagram was calculated for the measured bulk chemistry to model the near-peak metamorphic conditions, whereas the low-temperature side of the phase diagram was calculated using a new effective bulk chemistry in order to infer the retrograde conditions.

The presence of orthopyroxene + garnet in the peak assemblage constrains the stability of the peak assemblage at temperatures > 820°C at pressures > 7 kbar. The absence of orthopyroxene in the matrix assemblage suggest that the sample recrystallized and equilibrated within the Grt-Bt-Kfs-Pl-Qtz field on the retrograde *P-T* path. Petrographic observations, for example the straight grain boundaries between garnet and matrix biotite (Fig. 4b) suggest late garnet growth. In order to evaluate the garnet growth history of the sample, garnet modes were calculated and contoured molar quantities are plotted in Figure 7b. The plot demonstrates that the higher garnet mode occurs at higher pressures. With decreasing pressure, the garnet mode decreases and reach 0 around 7 kbar as garnet is being consumed (assuming isothermal decompression). The contours further illustrate that garnet growth will resume on near-isobaric cooling. The rim composition of garnet in contact with biotite indicates retrograde equilibrium condition of ca. 4.3-4.5 kbar and 630-640 ^{o}C (Fig. 8b). These conditions do, however, not correspond to the Grt-Bt field of the calculated phase diagram in Fig. 8a. This inconsistency might be related to uncertainties and accuracy in thermodynamic datasets and solution models. For example, the Grt-Bt field will expand to lower pressure conditions using the biotite solution model of Powell and Holland 1999 (instead of the solution model of White et al. 2007 which is used here) (field with dashed borders in Fig. 8a).

7. U-Pb zircon and monazite geochronology

7.1 Zircon results

Zircon is abundant and highly heterogeneous in all three samples investigated (garnet-sillimanite-cordierite gneiss; AHA240, AHA242 and garnet-biotite gneiss; AHA241). Each sample contains several subpopulations consisting of (i) equant subrounded grains, (ii) prismatic and variously resorbed grains, and (iii) prismatic euhedral crystals. The analyses were done on selections of prismatic euhedral to subhedral crystals. Three zircon grains of sample AHA242 Ma yield identical ^{206}Pb/^{238}U ages of about 566 Ma with a slight spread in ^{207}Pb/^{206}Pb age which may reflect small amounts of inherited zircon, or some later resetting (Fig. 9). This may be supported by the fact that the youngest analysis was obtained from an externally resorbed prism. The data sample AHA240 show the strongest spread with two euhedral tips defining concordant analyses at 572-570 Ma but another euhedral zircon tip yielding about 462 Ma. One of the prisms of sample AHA241 yields a discordant Precambrian age whereas two other prisms are concordant at 570-568 Ma, together defining a discordia line with intercept ages of 1038 ± 6 Ma and 569.8 ± 1.5 Ma (Fig. 9).

7.2 Monazite results

Monazite is present in all three samples in variable quantities, generally as equant, euhedral to anhedral grains. Two grains from each sample were analyzed, obtaining results that are concordant but very different from those of the zircons as they display a wide range of dates (Fig. 9). The two analyses of sample AHA242 yield both the oldest and youngest dates of 606 and 526 Ma. A monazite grain of sample AHA241 also yields an age of 591 Ma, older than that of the zircons. The other grain and the two in AHA240 are younger than the zircon.

8. Discussion

8.1 *P-T* path

The metamorphic evolution of the investigated rocks from Mühlig-Hofmannfjella in the form of a *P-T* path, is given in Fig. 10a. Chemical and textural evidence of the early prograde metamorphic evolution is generally difficult to recover in high-grade rocks, and this is also the case with supracrustal rocks studied herein. The calculated phase equilibria for the two modelled bulk composition are consistent and shows good agreement with the observed natural assemblages. Both samples record granulite facies metamorphism and the pseudosections suggest peak metamorphic temperatures ≥ 810-820 ºC at mid-crustal levels (ca. 8 kbar). The phase diagram and the presumed reaction history of the cordierite-bearing gneiss can be explained by a clockwise *P-T* path characterized by post-peak decompression from 8 kbar to about 4 kbar. The decrease in pressure from about 8 kbar to 4 kbar is equivalent to an uplift of about 15 km. In both samples, prograde garnets were consumed during decompression and resumed growth on the isobaric cooling segment of the *P-T* path (Fig. 10a).

The decompression segment is comparable to the *P-T* evolution recorded by garnet-orthopyroxene gneisses from Filchnerfjella (Engvik and Elvevold, 2004; Baba et al., 2008; Ravikant, 2009; Elvevold and Engvik, 2013), as well as other parts of central Dronning Maud Land (e.g. Bisnath and Frimmel, 2005; Board et al., 2005; Colombo and Talarico, 2004; Pant et al., 2013; Palmeri et al. 2018). This type of clockwise *P-T* paths is believed to be a key feature of the Pan-African tectonism (Harley, 2003). A *P-T* evolution involving a final isobaric cooling segment has also been proposed by Palmeri et al. (2018) for high-pressure granulites from Conradfjella, and by Pauly et al. (2016) for granulites from H.U. Sverdrupfjella.

8.2 Zircon and monazite growth

Given the morphological variability of the zircon population, the likely presence of old detrital zircon, and the long-lived thermal evolution of the region, it is reasonable to expect a considerable scatter in the zircon data. Somewhat surprisingly, this is not the case. One of the grains in AHA241 preserves an old Mesoproterozoic age, likely due to an original detrital component, but the remaining analyses all yield ages between 572 and 562 Ma. The data for AHA241 converge at 569.8 ± 1.5 Ma, three analyses of sample AHA242 indicates about 566 Ma, and two of AHA240 are about 570 Ma, but with a younger grain at 562 Ma. The dominant euhedral prismatic shape of the analyzed grains and their isotopic coherence suggests that there was a main event of crystallization at around 570 Ma.

The monazite results, on the other hand, indicate that the rocks were subjected to prolonged metamorphic conditions and/or were overprinted by later metamorphic events. Individual grains yield ages ranging from 606 to 526 Ma. There are several possible explanations for the pattern; (1) The monazite reflects prolonged crystallization, both earlier and later than zircon, and a late growth event (at ≤ 526 Ma) that partially recrystallized and/or overgrew earlier monazites creating the pattern of variable ages. The data shown in Fig. 9 may either be actual times of monazite growth, or they can represent mixing of different generations. Mixed age components in U-Pb-analyses in the simplest case give a discordia line where the maximum and minimum intercept indicate the respective ages of the two mixed components. The fact that these analyses do not define any such lines (because they are concordant) means that, if the ages are mixed, these age components are closer in age than the 526 and 606 Ma end member analyses. (2) Alternatively, the young monazite ages may be due to partial diffusion of Pb during permanence at protracted high temperature conditions (e.g. Gasser et al. 2015). The fact that the youngest dated grains in each sample are the smallest ones would seem to support this mechanism. The older dates of 606 and 591 Ma obtained for two of the grains, however, would seems to argue against simple diffusion. A possible explanation is that the latter may have been encapsulated in early grown minerals, hence preventing the build-up of a diffusive gradient in the grains and inhibiting diffusion. Either way, the monazite ages presented here show a prolonged history of these rocks, with monazite growth both prior to and after zircon crystallization at 570-566 Ma.

8.3 Comparison with previous geochronological data

Previous U-Pb zircon age data from Mühlig-Hofmannfjella are reported by Jacobs et al. (2003a, 2003b) and Baba et al. (2015) (Fig. 10b). Jacobs et al. (2003a, 2003b) identified Mesoproterozoic protolith ages in the range 1150-1000 Ma, as well as a Mesoproterozoic metamorphic age at 1061 ± 2 Ma. Similar ages are reported from Gjelsvikfjella (Jacobs et al., 2003a; 2003b; Bisnath et al., 2006), and from H.U. Sverdrupfjella (Board et al. 2005; Pauly et al., 2016). The Mesoproterozoic protolith and metamorphic ages are all from orthogneisses.

Baba et al. (2015) reported U-Pb zircon ages of 633 ± 4 Ma, 599 ± 1 Ma and 598 ± 2 Ma from garnet-sillimanite-cordierite gneisses from the northwestern side of Hochlinfjellet (Fig.10b). These ages are significantly older than the ca. 570 Ma zircon ages obtained in this study. It is, however, reasonable to assume that the samples studied by Baba et al. (2015) have experienced identical *P-T-t* evolution as the garnet-sillimanite-cordierite gneisses studied herein.

A deformed leucogranite from Hochlinfjellet yielded 558 ± 6 Ma (U-Pb zircon, Jacobs et al., 2003a, Fig.10b), which was interpreted as the crystallization age of a high-grade melt. The authors report an identical age of 557 ± 13 Ma for another leucosome at the nearby nunatak Festninga (Fig.10b). These ages are somewhat younger than the zircon ages recorded in our study, although comparable considering the analytical errors. Rim overgrowths of zircons from a charnockitic and a migmatitic gneiss record ages of 521 ± 2 Ma and 528 ± 10 Ma, respectively (Fig.10b). These ages are identical to the U-Pb zircon ages of 522-525 Ma from garnet-sillimanite-cordierite gneisses from Filchnerfjella (Baba et al. 2015). The latter metamorphic ages are significantly younger than the zircon ages obtained in this study but are comparable to the youngest monazite ages.

Jacobs et al. (1998) have reported U-Pb zircon age data from various lithologies from Orvinfjella and Wohlthatmassivet, located 200-250 km east of Hochlinfjellet. In addition to Mesoproterozoic protolith and metamorphic ages (ca. 1130 Ma and ca. 1080 Ma, respectively), two different metamorphic age groups at ca. 570-550 Ma and ca. 530-515 Ma were recorded. Other ages of ca. 570 Ma have been reported from H.U. Sverdrupfjella (Board et al. 2005; Pauly et al., 2016), Gjelsvikfjella (Bisnath et al., 2006) and Humboldtfjella (Mikhalsky et al., 1997).

Geochronological data on monazite are available from H.U. Sverdrupfjella (Board et al. 2005; Pauly et al. 2016) and Humboldtfjella (Pant et al., 2013). Board et al. (2005) report a U/Pb concordia SHRIMP age of 528 ± 6 Ma, whereas in-situ dating of monazite yielded an age of 544 ± 16 Ma which they interpret as the timing of retrograde amphibolite-facies reworking. The monazite data reported by Board et al. (2005) show an age scatter of a similar magnitude as our results. Their results did not reveal any systematic variation in ages as a function of the textural position of monazite in the sample (Board et al. 2005). Pauly et al. (2016) describe a felsic granulite with monazite dates that range from > 600 Ma to 420 Ma. Matrix monazites are for the most part younger than 570 Ma and yield an age peak at ca. 540 Ma which they interpret as recrystallization after decompression under high-temperature low-pressure conditions. Chemical in-situ dating of monazite from Humboldtfjella indicate growth between 640 and 580 Ma (Pant et al., 2013). A younger age group of ca. 540 Ma was interpreted as thermal overprint related to the emplacement of charnockite and A-type granites (Pant et al., 2013).

Monazite crystallizes over a wide range of *P-T* conditions and can grow during the prograde and retrograde segments during a single metamorphic cycle (e.g. Yakymchuk et al. 2017). Although they can have different interpretations, the monazite dates obtained in this study are comparable to ages recorded in previous studies (Board et al. 2005; Pant et al. 2013; Pauly et al. 2016) and reveal a pattern that is characteristic of the Pan-African evolution of central DML. Further detailed petrochronology work is needed in order to link the monazite and zircon growth to the *P-T* path by considering textural association of the accessory minerals along with geochemical characteristics.

8.4. Prolonged Pan-African metamorphic history

Geochronology demonstrates that the Maud Belt record a prolonged Ediacaran-Cambrian metamorphic history that span > 100 Myr (Fig. 10c). Early, pre-600 Ma metamorphic ages have been recorded in Schirmacheroasen (Baba et al., 2010), Mühlig-Hofmannfjella (Baba et al. 2015), Humboldtfjella (Pant et al. 2013), and in H.U. Sverdrupfjella (Pauly et al., 2016). Pauly et al. (2016) report zircon ages around 600 Ma, as well as > 600 Ma monazite inclusions in garnet, which they interpreted to date the onset of the Pan-African metamorphism. Likewise, Baba et al. (2015) interpreted the U-Pb zircon age of 633 ± 4 Ma from Mühlig-Hofmannfjella (Fig. 10b) to an early metamorphic stage. Accessory phases such as monazite and zircon may preserve sub-solidus, or early supra-solidus prograde metamorphic ages when the phases are included in prograde garnet and therefore protected from dissolution during later high-grade metamorphism and anatexis.

Post-600 Ma zircon and monazite age data record a large range of ages between 580-520 Ma (Jacobs et al., 2003b, 2008; Board et al., 2005; Bisnath et al. 2006; Pauly et al., 2016; Baba et al. 2015, this study). These ages can be interpreted as a result of one long-lived event, or the result of a metamorphic history that involves more than one thermal cycle. We have not observed any petrological indication in the studied samples for undergoing more than one thermal cycle, therefore we prefer to interpret the large range of metamorphic ages to indicate a prolonged metamorphic evolution. This study, as well as previous metamorphic *P-T* studies of Maud Belt rocks (e.g. Elvevold and Engvik, 2013; Bisnath and Frimmel, 2005; Pauly et al. 2016) have shown that peak pressures occurred before peak temperature, which is consistent with a relatively long residence time in the core of the orogen.

Crystallization of anatectic melt during cooling from peak temperature is, in fact, expected to be the main mechanism for zircon growth in supra-solidus metamorphic rocks (Yakymchuk et al. 2017). Scatter in U-Pb ages has been described in several studies of granulite facies rocks (e.g. Kunz et al., 2018; Rubatto et al., 2001; Diener et al., 2013). Rocks that have experienced identical *P-T* evolution, but variable amount of melt loss, will yield different solidus temperatures, which again can be an explanation for differences in zircon ages (Korhonen et al., 2013). Residual granulites and migmatite melanosome may for example contain zircons that have survived heating to peak temperatures, whereas migmatite leucosomes and anatectic granites are predicted to contain mostly newly formed zircon with minimal inherited components (Yakymchuk & Brown, 2014).

It has also been shown that zircon can grow directly from breakdown of other Zr-rich major phases such as garnet (Fraser et al, 1997, Degeling et al. 2001). We have shown herein that decompression along the *P-T* path resulted in garnet consumption (Fig.7), which may have released Zr for new zircon growth.

8.5. Heat source of the high-temperature metamorphism

Ediacaran-Cambrian high-grade and anatectic rocks are present along the length of the mountain range of DML; extending for more than 1500 km from H.U. Sverdrupfjella (0°) in the west to Lützow-Holmbukta (40-45°E) in the east. The regional-scale high-grade metamorphism and extensive magmatism over large areas, require a heat source capable of maintaining high temperatures for a long time (> 100 Myr). Possible explanations for such high heat flow into the crust are; i) advection of mantle heat by lithospheric extension and magmatism, and ii) radioactive decay of heat producing elements (U, Th and K). Other possibilities, such as shear heating, are not supposed to be significant on a regional scale (Clark et al., 2011).

The apparent absence of voluminous, coeval mafic or ultramafic rocks during granulite formation suggests that mantle magmatism is not a likely heat source for the observed high-grade metamorphism in DML. The syn- to late-tectonic granitoid intrusives, including charnockite, are more likely a crustal response to high temperature conditions rather than the cause of the metamorphism. The lack of mantle-derived magmatism suggests that the observed granulite facies metamorphism in DML is the result of radiogenic heat production. In this scenario, the high heat flow is a result of heat generated within the thickened crustal column during the Ediacaran-Cambrian collisional orogenesis.

It has been argued that crustal heat production by radioactive decay can be significant in thickened crust provided that the crust remains thickened over a long period of time (e.g. Clark et al., 2011; Korhonen et al., 2013; Kelsey and Hand, 2015; Horton et al., 2016). Numerical modelling of orogens has shown that crustal material with moderate levels of heat producing elements can reach temperatures in excess of 900°C if the crust is kept at depth over an extended period (Clark et al., 2011; Jamieson and Beaumont, 2011). Radioactive self-heating is maximized by high concentration of heat-producing elements and thick continental crust in long-lived orogens (Clark et al., 2011). In fact, in several regional UHT terranes, the burial of radioactive heat-producing elements has been interpreted as the primary driver of UHT metamorphism (Clark et al., 2015; Kelsey and Hand, 2015).

The wide range of recorded Ediacaran-Cambrian metamorphic dates in DML is consistent with a long-lived heat source. This fact, together with the absence of large-scale mafic magmatism, indicate the heat source for the observed granulite facies metamorphism is the result of radioactive heating at mid crustal depths.

8.6 Long-lived, hot orogens

The East African-Antarctic Orogen in Dronning Maud Land appears as a wide, hot orogen with > 100 Myr of tectonothermal activity. Similar prolonged high-grade metamorphism, and comparable ages, are reported from other Gondwana terranes including southern India

(Collins et al. 2014; Clark et al. 2015), Madagascar (Boger et al., 2015; Fitzsimons et al., 2016; Holder et al., 2018) and Sri Lanka (He et al., 2018). Even though the amalgamation of Gondwana is commonly discussed in terms of collisional suturing between east and west Gondwana, the assembly was most probably polyphase and involved a series of collisions between juvenile arc terranes and accretion of older continental fragments (Meert, 2003). Formation of the Gondwana supercontinent was thus long-lived and complex (e.g. Meert, 2003; Squire et al., 2006; Gray et al., 2008; Meert and Lieberman, 2008; Santosh et al., 2009; Collins et al., 2014; Abu-Alam et al., 2014; Clark et al., 2015; Horton et al., 2016; Fitzsimons, 2016; He et al., 2018).

9. Conclusion

The supracrustal gneisses from western Mühlig-Hofmannfjella, Maud Belt, record a prolonged metamorphic evolution that took place at high-temperature conditions during the Pan-African orogeny. Peak metamorphism reached granulite facies conditions ($T \geq 810$-$820^{o}C$) at mid-crustal levels (ca. 30 km) and resulted in partial melting. The peak stage was followed by near-isothermal exhumation to crustal depths of ca. 15 km and subsequent final isobaric cooling.

Available age data from central Dronning Maud Land suggest that continental collision may have started in the early Ediacaran (630-600 Ma) and ended in the Cambrian (ca. 520 Ma). The regional scale and long duration of high-temperature metamorphism in Dronning Maud Land are consistent with radiogenic heat accumulation beneath a long-lived orogenic plateau.

Acknowledgments

Samples for this study were collected during the Norwegian Antarctic Research Expedition 1996/97. We thank M. Erambert for help in the microprobe laboratory at University of Oslo and B. Willemoes-Wissing at the SEM laboratory at the Geological Survey of Norway. M. Flowerdew, J. Majka and V. Pease and two anonymous reviewers, are thanked for valuable and constructive comments on earlier versions of the manuscript.

References

Abu-Alam, T.S., Hassan, M., Stüwe, K., Meyer, S.E. & Passchier, C.W., 2014. Multistage tectonism and metamorphism during Gondwana collision: Baladiyah Complex, Saudi Arabia. Journal of Petrology, 55, 1941–1964.

Baba, S., Owada, M., and Shiraishi, K. 2008. Contrasting metamorphic P-T path between Schirmacher Hills and Mühlig-Hofmannfjella, central Dronning Maud Land, East Antarctica. In Satish-Kumar, M.; Motoyoshi, Y.; Osanai, Y.; Hiroi, Y.; and Shiraishi, K., eds. Geodynamic evolution of East Antarctica: a key to the East-West Gondwana connection. Geol. Soc. Lond. Spec. Publ., 308, 401–417.

Baba, S., Hokada, T., Kaiden, H., Dunkley, D.J., Owada, M., Shiraishi, K., 2010. SHRIMP zircon U-Pb dating of sapphirine-bearing granulite and biotite-hornblende gneiss in the Schirmacher Hills, east Antarctica: implications for Neoproterozoic ultrahigh-temperature metamorphism predating the assembly of Gondwana. Journal of Geology, 118, 621–639.

Baba, S., Horie, K., Hokada, T., Owada, M., Adachi, T., Shiraishi, K., 2015. Multiple collisions in the East African-Antarctic Orogen: Constraints from timing of metamorphism in the Filchnerfjella and Hochlinfjellet terranes in central Dronning Maud Land. Journal of Geology, 123, 55-78.

Bartoli, O., 2017. Phase equilibria modelling of residual migmatites and granulites: An evaluation of the melt-reintegration approach. Journal of Metamorphic Geology, 35, 919-942.

Bisnath, A., Frimmel, H.E., 2005. Metamorphic evolution of the Maud Belt: P-T-t path for high-grade gneisses in Gjelsvikfjella Dronning Maud Land, East Antarctica. Journal of African Earth Sciences, 43, 505-524.

Bisnath, A., Frimmel, H.E., Armstrong, R.A., Board, W.S., 2006. Tectono-thermal evolution of the Maud Belt: new SHRIMP U-Pb zircon data from Gjelsvikfjella, Dronning Maud Land, East Antarctica. Precambrian Research, 150, 95–121.

Board, W.S., Frimmel, H.E., Armstrong, R.A., 2005. Pan-African tectonism in the Western Maud Belt: P-T-t path for high-grade gneisses in the H.U. Sverdrupfjella, East Antarctica. Journal of Petrology, 46, 671-699.

Boger, S.D., Hirdes, W., Ferreira, C.A.M., Jenett, T., Dallwig, R., Fanning, C.M., 2015. The 580-520 Gondwana suture of Madagascar and its continuation into Antarctica and Africa. Gondwana Research, 28, 1048-1060. http://dx.doi.org/10.1016/j.gr.2014.08.017

Bucher, K., Frost, B.R., 2005. Fluid transfer in high-grade metamorphic terrains intruded by anorogenic granites: the Thor range, Antarctica. Journal of Petrology 47, 567-593.

Clark, C., Fitzsimons, I.C.W., Healy, D., Harley, S.L., 2011. How does the continental crust get really hot? Elements, 7, 235-240

Clark, C., Healy, D., Johnson, T., Collins, A.S., Taylor, R.J., Santosh, M., Timms, N.E., 2015. Hot orogens and supercontinent amalgamation: A Gondwana example from southern India. Gondwana Research, 28, 1310-1328. https://doi.org/10.1016/j.gr.2014.11.005

Collins, A.S., Pisarevsky, S.A., 2005. Amalgamating eastern Gondwana: The evolution of Circum-Indian Orogens. Earth Science Reviews, 71, 229-270.

Collins, A.S., Clark, C., Plavsa, D., 2014. Peninsular India in Gondwana: The tectonothermal evolution of the Southern Granulite Terrane and its Gondwanan counterparts. Gondwana Research, 25, 190–203

Colombo, F., Talarico, F., 2004. Regional metamorphism in the high-grade basement of Central Dronning Maud Land, East Antarctica. Geologische Jahrbuch B96, 7-47.

Connolly, J.A.D., 2009. The geodynamic equation of state: What and how. Geochemistry, Geophysics, Geosystems, 10, Q10014

Connolly, J.A.D., Kerrick, D.M., 1987. An algorithm and computer program for calculating composition phase diagrams. CALPHAD 11, 1-55.

Corfu, F., 2004. U-Pb age, setting and tectonic significance of the anorthosite-mangerite-charnockite-granite suite, Lofoten-Vesterålen, Norway: Journal of Petrology 45, 1799-1819, https://doi: 10.1093/petrology/egh034

D'Souza, M.J., Prasad, A.V.K., Ravindra, R., 2006. Genesis of ferropotassic A-type granitoid of Mühlig-Hofmannfjella, Central Dronning Maud Land, East Antarctica. In: Fütterer, D.K., Damaske, D., Kleinschmidt, G., Miller, H., Tessensohn, F. (Eds) Antarctica: Contributions to Global Earth Sciences, Springer Verlag Berlin Heidelberg, 45-54.

Degeling, H., Eggins, S., Ellis, D.G., 2001. Zr budgets for metamorphic reactions, and the formation of zircon from garnet breakdown. Mineral Magazine, 65, 749-758.

Diener, J.F., White, R.W., Link, K., Dreyer, T.S., Moodley, A., 2013. Clockwise, low-P metamorphism of the Aus granulite terrain, southern Namibia, during the Mesoproterozoic Namaqua Orogeny. Precambrian Research, 224, 629–652

Elvevold, S., Engvik A.K., 2013. Pan-African decompressional P-T path recorded by granulites from central Dronning Maud Land, Antarctica. Mineralogy and Petrology, 107, 651-664.

Engvik, A.K., Elvevold, S., 2004. Pan-African extension and near-isothermal exhumation of a granulite facies terrain, Dronning Maud Land, Antarctica. Geological Magazine, 141, 1-12.

Engvik, A.K., Kalthoff, J., Bertram, A., Stöckhert, B., Austrheim, H., Elvevold, S., 2005. Magma-driven hydraulic fracturing and infiltration of fluids into the damaged host rock an example from Dronning Maud Land, Antarctica. Journal of Structural Geology, 27, 839-854.

Engvik, A.K., Stöckhert, B., 2007. The inclusion record of fluid evolution crack healing and trapping from a heterogeneous system during rapid cooling of pegmatitic veins (Dronning Maud Land; Antarctica). Geofluids, 7, 171-185.

Engvik, L., Stöckhert, B., Engvik, A.K., 2009. Fluid infiltration, heat transport, and healing of microcracks in the damage zone of magmatic veins: Numerical modeling. Journal of Geophysical Research, 114, B05203, https://doi:10.1029/2008JB005880

Fitzsimons, I.C.W., 2016. Pan-African granulites of Madagascar and southern India: Gondwana assembly and parallels with modern Tibet. Journal of Mineralogical and Petrological Sciences, 111, 73-88. https://doi.org/10.2465/jmps.151117.

Fraser, G., Ellis, D., Eggins, S. 1997. Zirconium abundance in granulite-facies minerals, with implications for zircon geochronology in high-grade rocks. Geology, 25, 607-610

Fritz, H., Abdelsalam, M., Ali, K.A., Bingen, B., Collins, A.S., Fowler, A.R., Ghebreab, W., Hauzenberger, C.A., Johnson, P.R., Kusky, T.M., Macey, P., Muhongo, S., Stern, R.J., Viola, G., 2013. Orogen styles in the East African Orogen: A review of the Neoproterozoic to Cambrian tectonic evolution. Journal of African Earth Sciences, 86, 65-106.

Fuhrman, M.L., Lindsley, D.H., 1988. Ternary-feldspar modeling and thermometry. American Mineralogist, 75, 201-215.

Gasser, D., Jeřábek, P., Faber, C., Stünitz, H., Menegon, L., Corfu, F., Erambert, M. Whitehouse, M.J., 2015. Behavior of geochronometers and timing of metamorphic reactions during deformation at lower crustal conditions: phase equilibrium modelling and U–Pb dating of zircon, monazite, rutile and titanite from the Kalak Nappe Complex, northern Norway. Journal of Metamorphic Geology, https://doi:10.1111/jmg.12131

Grantham, G.H., Manhica, A.D.S.T., Armstrong, R.A., Kruger, F.J., Loubser, M., 2011. New SHRIMP, Rb/Sr and Sm/Nd isotope and whole rock chemical data from central Mozambique and western Dronning Maud land, Antarctica: Implications for the nature of the eastern margin of the Kalahari Craton and the amalgamation of Gondwana. Journal of African Earth Sciences, 59, 74–100.

Gray, D.R., Foster, D.A., Meert, J.G., Goscombe, B.D., Armstrong, R., Trouw, R.A., Passchier, C.W., 2008. A Damara orogen perspective on the assembly of southwestern Gondwana. Geological Society, London, Special Publications 294, 257–278.

Grosch, E., Frimmel, H., Abu-Alam, T.S., Kosler J., 2015. Metamorphic and age constraints on crustal reworking in the western H.U. Sverdrupfjella: Implications for the evolution of Western Dronning Maud Land, Antarctica. Journal of the Geological Society, 172, 499-518.

Harley, S.L., 2003. Archaean-Cambrian crustal development in East Antarctica: Metamorphic characteristics and tectonic implications. In: Yoshida, M., Windley, B.F., Dasgupta, S. (Eds.) Proterozoic East Gondwana: Supercontinent Assembly and Breakup, Geological Society of London Special Publication 206, 203-230.

He, X.F., Hand, M., Santosh, M., Kelsey, D.E., Morrissey, L.J., Tsunogae, T., 2018. Long-lived metamorphic P-T-t evolution of the Highland Complex, Sri Lanka: Insights from mafic granulites. Precambrian Research, 316, 227-243. https://doi.org/10.1016/j.precamres.2018.08.008

Hendriks, B.W.H., Engvik, A.K., Elvevold, S., 2013. ^{40}Ar/^{39}Ar record of late Pan-African exhumation of a granulite facies terrain, central Dronning Maud Land, East Antarctica. Mineralogy and Petrology 107, 665-677.

Henjes-Kunst, F., 2004. Further evidence for Pan-African polyphase magmatism and metamorphism in central Dronning Maud Land, East Antarctica, from rocks at Schirmacheroase: a geochronological study. Geologisches Jahrbuch B96, 255-291.

Holland, T., Powell, R., 1996. Thermodynamics of order–disorder in minerals: I. Symmetric formalism applied to minerals of fixed composition. American Mineralogist 81, 1413–1424.

Holland, T.J.B., Powell, R., 1998. An internally consistent thermodynamic dataset for phases of petrological interest. Journal of Metamorphic Geology 16, 309–343.

Holland, T.J.B., Powell, R., 2001. Calculation of phase relations involving haplogranitic melts using an internally consistent thermodynamic dataset. Journal of Petrology 42, 673-683.

Holland, T.J.B, Powell, R., 2011. An improved and extended internally consistent thermodynamic dataset for phases of petrological interest, involving a new equation of state for solids. Journal of Metamorphic Geology, 29, 333-383. https://doi.org/10.1111/j.1525-1314.2010.00923.x

Horton, F., Hacker, B., Kylander-Clark. A., Holder, R., Jöns, N., 2016. Focused radiogenic heating of middle crust caused ultrahigh temperatures in southern Madagascar. Tectonics, 35, 293-314. https://doi.org/10.1002/2015TC004040

Jacobs. J., Fanning, C.M., Henjes-Kunst, F., Olesch, M., Paech, H.-J., 1998. Continuation of the Mozambique Belt into East Antarctica: Grenville-age metamorphism and polyphase Pan-African high-grade events in Central Dronning Maud Land. Journal of Geology 106, 385-406

Jacobs, J., Bauer, W., Fanning, C.M., 2003a. New age constraints for Grenville-age metamorphism in western central Dronning Maud Land (East Antarctica), and implications for the paleogeography of Kalahari in Rodinia. International Journal of Earth Sciences 92, 301–315.

Jacobs, J., Bauer, W., Fanning, C.M., 2003b. Late Neoproterozoic/Early Palaeozoic events in central Dronning Maud Land and significance for the southern extension of the East African Orogen into East Antarctica. Precambrian Research 126, 27-53

Jacobs, J., Bingen, B., Thomas, R.J., Bauer, W., Wingate, M.T.D., Feitio, P., 2008. Early Paleoproterozoic orogenic collapse and voluminous late tectonic magmatism in Dronning Maud Land and Mozambique: insight into the partially delaminated orogenic root of the East African-Antarctic Orogen? In: Satish-Kumar, M., Motoyoshi, Y., Osanai, Y., Hiroi, Y., Shiraishi, K., (Eds.) Geodynamic evolution of East Antarctica: a key to the East-West Gondwana connection. Geological Society London Special Publication 308, 69–90.

Jaffey, A. H., Flynn, K. F., Glendenin, L. E., Bentley, W. C., Essling, A. M., 1971. Precision measurement of half-lives and specific activities of U-235 and U-238: Physical Review C, 4, 1889.

Jamieson, R.A., Beaumont, C., 2011. Coeval thrusting and extension during lower crustal ductile flow – implications for exhumation of high-grade metamorphic rocks. Journal of Metamorphic Geology, 29, 33-51. https://doi.org/10.1111/j.1525-1314.2010.00908.x

Kelsey, D.E., Hand, M., 2015. On ultrahigh temperature crustal metamorphism: Phase equilibria, trace element thermometry, bulk composition, heat sources, timescales and tectonic settings. Geoscience Frontiers, 6, 311-356. https://doi.org/10.1016/j.gsf.2014.09.006

Kennedy, W.Q., 1964. The structural differentiation of African in the Pan-African (+- 500 m.y.) tectonic episode. 8th Annual Report of the Research Institute of African Geology, University of Leeds, UK, 48-49.

Korhonen, F.J., Clark, C., Brown, M., Bhattacharya, S., Taylor, R., 2013. How long-lived is ultrahigh temperature (UHT) metamorphism? Constraints from zircon and monazite geochronology in the Eastern Ghats orogenic belt, India. Precambrian Research. https://doi.org/10.1016/j.precamres.2012.12.001

Krogh, T. E., 1973. A low-contamination method for hydrothermal decomposition of zircon and extraction of U and Pb for isotopic age determinations: Geochimica et Cosmochimica Acta 37, 485-494, doi: http://dx.doi.org/10.1016/0016-7037(73)90213-5.

Kröner, A., Stern, R.J., 2005. Pan-African orogeny. Encyclopedia of Geology (2004), 1, 1-12

Kunz, B.E., Regis, D., Engi, M., 2018. Zircon ages in granulite facies rocks: decoupling from geochemistry above 850°C? Contribution to Mineralogy and Petrology, 173, 26, https://doi.org/10.1007/s00410-018-1454-5

Ludwig, K.R., 2009. Isoplot 4.1. A geochronological toolkit for Microsoft Excel, Berkeley Geochronology Center Special Publications, Volume 4.

Markl, G., Piazolo, S., 1998. Halogen-bearing minerals in syenites and high-grade marbles of Dronning Maud Land, Antarctica: self-retrogression of originally anhydrous rocks by late-magmatic fluids and modelling of their chemical, thermal and isotope evolution

Markl, G., Henjes-Kunst, F., 2004. Magmatic conditions of formation and autometasomatism of post-kinematic charnockites in Central Dronning Maud Land, East Antarctica. Geologische Jahrbuch B96, 139-188.

Mattinson, J. M., 2005, Zircon U-Pb chemical abrasion ("CA-TIMS") method: Combined annealing and multi-step partial dissolution analysis for improved precision and accuracy of zircon ages: Chemical Geology, v. 220, no. 1-2, p. 47-66, doi: http://dx.doi.org/10.1016/j.chemgeo.2005.03.011

Meert, J.G., 2003. A synopsis of events related to the assembly of Eastern Gondwana. Tectonophysics 362, 1-40.

Meert, J.G., Lieberman, B.S., 2008. The Neoproterozoic assembly of Gondwana and its relationship to the Ediacaran–Cambrian radiation. Gondwana Research 14, 5–21.

Mikhalsky, E.V., Beliatsky, B.V., Savva, E.V., Wetzel, H.-U., Fedorov, L.V., Weiser, T. & Hahne, K. 1997. Reconnaissance geochronological data on polymetamorphic and igneous rocks of the Humboldt Mountains, central Queen Maud Land, East Antarctica. In: Ricci, C.A. (ed.) *The Antarctic Region: Geological Evolution and Processes.* Terra Antarctica Publication, Siena, 45-53

Ohta, Y., Tørudbakken, B.O., Shiraishi, K., 1990. Geology of Gjelsvikfjella and western Mühlig-Hofmannfjella, Dronning Maud Land, East Antarctica. Polar Research, 8, 99-126.

Ohta, Y., (ed) 1999. Nature environment map: Gjelsvikfjella and Western Mühlig-Hofmannfjella, Dronning Maud Land, Antarctica 1:100.000 – Sheets 1 and 2. With explanatory text, 37 pp. Norsk Polarinstitutt Temakart 24.

Palmeri, R., Godard, G., Di Vincenzo, G., Sandroni, S., Talarico, F.M., 2018. High-pressure granulite-facies metamorphism in central Dronning Maud Land (East Antarctica): Implications for Gondwana assembly. Lithos 300-301, 361-377. https://doi.org/10.1016/j.lithos.2017.12.014

Pant N.C., Kundu A., D'Souza M.J., Saikia A. 2013. Petrology of the Neoproterozoic granulites from Central Dronning Maud Land, East Antarctica – Implications for

southward extension of East African Orogen (EAO). Precambrian Research 227, 389-408.
Paulsson, O., 2003. U-Pb geochronology of tectonothermal events related to the Rodenia and Gondwana supercontinents – observations from Antarctica and Baltica. Litholund theses 2, Lund University, Sweden.
Paulsson, O., Austrheim, H., 2003. A geochronological and geochemical study of rocks from the Gjelsvikfjella, Dronning Maud Land, Antarctica – implications for Mesoproterozoic correlations and assembly of Gondwana. Precambrian Research, 125, 113-138.
Pauly, J., Marschall, H.R., Meyer, H.P., Chatterjee, N., Monteleone, B., 2016. Prolonged Ediacaran-Cambrian metamorphic history and short-lived high-pressure granulite-facies metamorphism in the H.U. Sverdrupfjella, Dronning Maud Land (East Antarctica): Evidence for continental collision during Gondwana assembly. Journal of Petrology, 57, 185-228.
Pouchou, J.P., Pichoir, 1984. Cameca PAP program. La Recherche Aerospatiale, 3, 167-192.
Powell, R., Holland, T.J.B., 1988. An internally consistent thermodynamic dataset with uncertainties and correlations: 3. Application to geobarometry, worked examples and a computer program. Journal of Metamorphic Geology, 6, 173-204.
Powell, R., Holland, T.J.B., 1999. Relating formulations of the thermodynamics of mineral solid solutions: activity modelling of pyroxenes, amphiboles and micas. American Mineralogist 84, 1-14.
Ravikant, V., Laux, J.H., Pimentel, M.M., 2007. Sm-Nd and U-Pb isotopic constraints for crustal evolution during Late Neoproterozoic from rocks of the Schirmacher Oasis, East Antarctica: geodynamic development coeval with the East African Orogeny. In: Cooper, A.K., Raymond, C.R. et al. (Eds.) A Keystone in a Changing World-Online

Proceedings of the 10th ISAES, edited by USGS Open-File Report 2007-1047, Short Research Paper 007, 5 p.; https://doi:10.3133/of2007-1047.srp007.

Ravikant, V., 2009. Tectono-metamorphic history recorded in high-grade rocks from Filchnerfjella: Further evidence for Pan-African reworking of the Grenville aged crust in central Dronning Maud Land, East Antarctica. Indian Journal of Geosciences 63, 1-12.

Rubatto, D., Williams, I.S., Buick, I.S., 2001. Zircon and monazite response to prograde metamorphism in the Reynolds Range, central Australia. Contribution to Mineralogy and Petrology, 140, 458–468

Santosh, M., Maruyama, S., Yamamoto, S., 2009. The making and breaking of supercontinents: some speculations based on superplume, superdownwelling and the role of tectosphere. Gondwana Research 15 (3–4), 324–341.

Squire, R.J., Campbell, I.H., Allen, C.M., Wilson, C.J.L., 2006. Did the Transgondwanan Supermountain trigger the explosive radiation of animals on Earth? Earth and Planetary Science Letters 250, 116–133.

Stern, R.J., 1994. Arc assembly and continental collision in the Neoproterozoic East African Orogeny: implications for the consolidation of Gondwanaland. Annual Reviews Earth Planetary Sciences 22, 319-351

Walsh, A.K., Kelsey, D.E., Kirkland, C.L., Hand, M., Smithies, R.H., Clark, C., Howard, H.M., 2015. P-T-t evolution of a large, long-lived, ultrahigh-temperature Grenvillian belt in central Australia. Gondwana Research, 28, 531-564. https://doi.org/10.1016/j.gr.2015.05.012

White, R. W., Powell, R., Holland, T. J. B., 2001. Calculation of partial melting equilibria in the system Na_2O–CaO–K_2O–FeO–MgO–Al_2O_3–SiO_2–H_2O (NCKFMASH). Journal of Metamorphic Geology 19, 139–153.

White, R. W., Powell, R., Holland, T. J. B., 2007. Progress relation to calculation of partial melting equilibria for metapelites. Journal of Metamorphic Geology, 25, 511-527.

White, R.W, Powell, R., Holland, T. J. B, Johnson, T.T., Green, E.C.R., 2014. New mineral activity-composition relations for thermodynamic calculations in metapelitic systems. Journal of Metamorphic Geology, 32, 261-286. https://doi.org/10.1111/jmg.12071

Whitney, D.L., Evans, B.W., 2010. Abbreviations of names of rock-forming minerals. American Mineralogist 95, 185-187.

Yakymchuk, C., Brown, M., 2014. Behavior of zircon and monazite during crustal melting. Journal of Geological Society of London, 171, 465-479

Yakymchuk, C., Clark, C., White, R.W., 2017. Phase relations, reaction sequences and petrochronology. In: Kohn, M.J., Engi, M and Lanari, P (Eds.) Petrochronology: Methods and Applications. Reviews in Mineralogy and Geochemistry 83, 13-53.

Figure captions

Figure 1. a) and b) The study area is located in Mühlig-Hofmannfjella in central Dronning Maud Land. c) Geological map of Mühlig-Hofmannfjella after Ohta (1999).

Figure 2. a) The supracrustal rocks outcrop in the low-lying areas between Hoggestabben and Hochlinfjellet. b) The foliated supracrustal gneisses are intruded by charnockite. Fluids released from the gneisses have caused a bleached alteration zone in the charnockite along the intrusive contact. c) The pelitic gneisses are associated with calc-silicate rocks and garnet-biotite gneisses. d) Garnet-sillimanite-cordierite gneisses are characterized by brownish weathering and foliation-parallel anatectic veins. e) Neosome in garnet-sillimanite-cordierite gneiss.

Figure 3. Photomicrographs of garnet-sillimanite-cordierite gneiss (a-e) and garnet-biotite gneiss (f). a) Garnet are present in two textural varieties; as larger anhedral inclusion-rich grains (Grt_1) and as smaller euhedral to subhedral grains (Grt_2). The large garnet is mantled by a moat of cordierite. The arrow points to a resorption embayment where garnet is replaced by secondary sillimanite and biotite. b) Small, secondary garnets, Grt_2, include cordierite. c) A euhedral sillimanite crystal (Sil_1) is surrounded by secondary fibrolitic sillimanite (Sil_{1sec}) along the grain boundaries. d) Spinel and sillimanite are overgrown and replaced by cordierite. e) Feldspar with low dihedral angel is interpreted to represent late crystallization of partial melts. f) The garnet-biotite gneiss contains a higher proportion of biotite than the sillimanite and cordierite bearing gneiss. Orthopyroxene is present as small inclusions in poikiloblastic garnet.

Figure 4. a) Biotite-quartz intergrowth and very fine-grained symplectite in contact with garnet. b) Secondary garnet displays straight grain boundaries towards biotite and irregular boundary in contact with quartz.

Figure 5. Calculated T-M_{H2O} pseudosection for a) garnet-cordierite-sillimanite gneiss (AHA245) and b) garnet-biotite gneiss (AHA244) at constant pressure of 8 kbar. All fields include quartz and ilmenite in addition to the listed phases. Higher variance field are shown by progressively darker shading. The stars indicate the lowest temperature for the stability of the near-peak assemblages. The bulk composition for AHA245 is (wt%); SiO_2: 66.80, Al_2O_3: 16.90, FeO: 7.04, MgO: 2.08, CaO: 1.42, Na_2O: 1.52, K_2O: 2.18. The bulk composition for AHA244 is (wt%); SiO_2: 63.00, Al_2O_3: 16.40, FeO: 5.59, MgO: 3.31, CaO: 4.30, Na_2O: 2.21, K_2O: 2.16.

Figure 6. a) Pseudosection calculated for garnet-sillimanite-cordierite gneiss (AHA245) in the NCKFMASHTO system with the adjusted H_2O content of 2.7 mol%. All fields include

quartz, two feldspars, ilmenite and magnetite in additional to the listed phases. Higher variance field are shown by progressively darker shading. The points A (A’), B, C and D in the diagram are constrained by textural relationships. The peak- or near-peak assemblage, point (A) plot in the Grt-Bt-Sil-Liq field (or alternatively in the Grt-Sil-Liq field – (A’)). This assemblage is replaced by cordierite-bearing assemblages (B). Breakdown of sillimanite to produce cordierite document further decompression and progression into the Crd-Grt-Liq field (C). Secondary growth of garnet, sillimanite and biotite reflect cooling into the field Grt-Bt-Sil (D). b) The diagram shows the modelled isopleths of Ca/(Ca+Fe+Mg) in Grt and Ca/(Ca+Na+K) in Pl. The isopleth for the measured composition of Grt_1 core and plagioclase inclusion intersects (red star) within the Grt-Bt-Sil-Liq field (shaded area) and indicate equilibrium conditions of ca. 8 kbar and 810°C.

Figure 7. a) P-T diagram contoured for molar quantities of garnet in sample AHA245. The plot demonstrates that a small amount of garnet will grow along an isobaric cooling path in the temperature range 740-720°C. b) Contoured molar quantities of garnet in sample AHA244. The highest garnet mode occurs at higher pressures and decreases with decreasing pressure. The contours show that garnet will start to grow again on isobaric cooling.

Figure 8. Pseudosection of sample AHA244 calculated in the NCKFMASHT system with the adjusted H_2O content of 1.9 mol%. The high-T side of the phase diagram was calculated for the measured bulk chemistry to model the near-peak metamorphic conditions, whereas the low-T side of the phase diagram was calculated using a new effective bulk chemistry in order to infer the retrograde conditions. The presence of orthopyroxene in the peak assemblage constrains the peak metamorphic temperatures > 820°C. b) The low-T part of the diagram

shows modelled isopleths of X_{Alm} in Grt_2 and Fe/(Fe+Mg) in Bt_2. The isopleths intersect at 4.3-4.5 kbar and 640-630°C.

Figure 9. U-Pb concordia diagrams and plane light photographs of monazite and zircon grains from the analyzed samples. Error ellipses show 2 sigma errors.

Figure 10. a) The estimated *P-T* path for supracrustal rocks from Vedskålen. b) Map showing published U-Pb ages from Festninga and Hochlinfjellet by Jacobs et al. (2003a)(J2003a), Jacobs et al. (2003b)(J2003b) and Baba et al. (2015)(B2015). c) Summary of temperature-time evolution of central Dronning Maud Land. The onset of Pan-African metamorphism is indicated by zircon and monazite ages that fall in the range 640-600 Ma. Peak metamorphism is interpreted to have occurred around 570-550 Ma, whereas exhumation and final cooling took place in the period 530-435 Ma.

Table 1

Representative microprobe garnet analyses (formula calculated on the basis of 12 oxygens)

Lithology	grt-sil-crd gneiss	grt-sil-crd gneiss	grt-sil-crd gneiss	grt-sil-crd gneiss	grt-sil-crd gneiss	grt-sil-crd gneiss	grt-bt gneiss	grt-bt gneiss	grt-bt gneiss
Sample	AHA245	AHA245	AHA245	AHA245	AHA240	AHA240	AHA244	AHA244	AHA244
Anal, no,	94	99	100	103	13	19	5	59	54
Type	core Grt_1	rim Grt_1	core Grt_2	rim Grt_2	core Grt_2	rim Grt_2	core	rim	rim cont bt
SiO_2	37,10	37,42	36,74	36,89	36,51	36,69	37,80	37,59	36,92
TiO_2	0,01	0,03	b.d.l	b.d.l	b.d.l	0,01	b.d.l	0,01	0,04
Al_2O_3	21,12	21,01	21,00	20,70	21,00	20,68	21,39	21,55	21,07
FeO	35,91	36,19	37,02	36,76	36,80	38,10	31,52	31,67	33,97
MnO	0,47	0,55	0,47	0,63	0,61	0,71	1,17	1,24	1,52
MgO	4,15	3,67	3,43	2,97	3,36	2,54	5,98	5,63	3,84
CaO	1,09	1,09	1,08	1,09	1,14	1,09	2,15	2,22	2,12
Cr_2O_3	0,07	0,16	0,08	0,13	0,08	0,16	0,11	0,02	0,08
Total	99,92	100,15	99,98	99,24	99,73	100,12	100,25	100,02	99,68
Si	2,973	3,002	2,963	3,003	2,955	2,976	2,974	2,968	2,966
Al	1,995	1,987	1,997	1,987	2,004	1,978	1,984	2,006	1,996
Ti	0,001	0,002	-	-	-	0,001	-	0,001	0,002
Fe^{3+}	0,054	-	0,072	-	0,082	0,059	0,060	0,056	0,064
Fe^{2+}	2,352	2,428	2,426	2,503	2,409	2,526	2,014	2,035	2,219
Mn	0,032	0,037	0,032	0,043	0,042	0,049	0,078	0,083	0,104
Mg	0,496	0,439	0,412	0,360	0,405	0,307	0,701	0,662	0,459
Ca	0,094	0,094	0,093	0,095	0,099	0,095	0,181	0,188	0,182
Cr	0,004	0,010	0,005	0,008	0,005	0,010	0,007	0,001	0,005
X_{grs}	0,032	0,031	0,031	0,032	0,034	0,032	0,061	0,063	0,061
X_{sps}	0,011	0,012	0,011	0,014	0,014	0,016	0,026	0,028	0,035
X_{alm}	0,791	0,810	0,819	0,834	0,815	0,849	0,677	0,686	0,749
X_{prp}	0,167	0,146	0,139	0,120	0,137	0,103	0,236	0,223	0,155
Fe/(Fe+Mg)	0,83	0,85	0,85	0,87	0,86	0,89	0,74	0,75	0,83

Table 2

Representative microprobe biotite analyses (formula calculated on the basis of 11 oxygens)

Lithology	grt-sil-crd gneiss	grt-sil-crd gneiss	grt-sil-crd gneiss	grt-sil-crd gneiss	grt-bt gneiss	grt-bt gneiss	grt-bt gneiss
Sample	AHA240	AHA240	AHA240	AHA245	AHA244	AHA244	AHA244
Anal, no,	40	23	26	35	11	3	52
Type	incl Grt_1	matrix	incl Kfs	matrix	matrix	incl grt	cont w grt
SiO_2	34,81	34,53	34,19	34,47	36,64	38,27	36,92
TiO_2	3,17	4,07	5,35	3,86	2,59	2,04	2,74
Al_2O_3	19,26	18,65	17,37	18,80	16,66	16,55	16,79
FeO	16,79	21,60	21,86	21,40	15,28	10,80	15,17
MnO	b.d.l	0,02	0,01	b.d.l	0,02	b.d.l	0,03
MgO	10,55	6,52	6,72	7,10	13,96	18,20	13,86
CaO	0,02	b.d.l	b.d.l	b.d.l	b.d.l	b.d.l	b.d.l
Na_2O	0,20	0,08	0,09	0,13	0,12	0,62	0,13
K_2O	9,68	9,75	9,87	9,78	9,41	8,19	9,45
Cr_2O_3	0,18	0,25	0,35	0,10	0,11	0,14	0,07
Total	94,66	95,48	95,80	95,64	94,81	95,00	95,16
Si	2,644	2,664	2,644	2,652	2,750	2,775	2,757
Al	1,725	1,697	1,584	1,705	1,474	1,415	1,479
Ti	0,181	0,236	0,311	0,223	0,146	0,111	0,154
Fe^{3+}	-	-	-	-	0,007	0,098	0,000
Fe^{2+}	1,067	1,394	1,414	1,377	0,952	0,556	0,947
Mn	-	0,001	0,001	-	0,001	-	0,002
Mg	1,194	0,750	0,774	0,814	1,562	1,967	1,543
Ca	0,002	-	-	-	-	-	-
Na	0,029	0,012	0,013	0,019	0,017	0,087	0,019
K	0,938	0,960	0,974	0,960	0,901	0,758	0,900
Cr	0,011	0,015	0,021	0,006	0,007	0,008	0,004
Fe/(Fe+Mg)	0,47	0,65	0,65	0,63	0,38	0,22	0,38

Table 3

Representative microprobe cordierite analyses
(formula calculated on the basis of 18 oxygens)

Lithology	grt-sil-crd gneiss	grt-sil-crd gneiss	grt-sil-crd gneiss
Sample	AHA240	AHA240	AHA245
Anal, no,	25	33	33
Type	matrix	w/spl incl	matrix
SiO_2	48,07	47,69	48,07
TiO_2	b.d.l	0,01	b.d.l
Al_2O_3	32,38	32,55	32,85
FeO	10,11	9,67	10,05
MnO	0,06	0,03	0,05
MgO	7,41	7,58	7,35
CaO	0,01	b.d.l	0,01
Na_2O	0,10	0,10	0,13
Total	98,25	97,75	98,54
Si	4,989	4,964	4,967
Al	3,962	3,994	4,001
Ti	-	0,001	-
Fe^{3+}	0,082	0,096	0,091
Fe^{2+}	0,796	0,746	0,777
Mn	0,005	0,003	0,004
Mg	1,146	1,176	1,132
Ca	0,001	-	0,001
Na	0,02	0,02	0,03

Table 4

Representative microprobe of additional phases

Lithology	grt-bt gneiss	grt-bt gneiss	grt-sil-crd gneiss	grt-sil-crd gneiss
Sample	AHA244	AHA244	AHA245	AHA245
Anal. no.	50	2	107	110
Mineral	pl	opx incl grt	spl incl crd	pl
SiO_2	56,63	51,08	0,05	59,39
TiO_2	0,01	0,06	0,02	0,02
Al_2O_3	27,62	1,99	56,06	25,87
FeO	b.d.l	25,98	29,95	b.d.l
MnO	b.d.l	0,27	0,03	0,02
ZnO	b.d.l	b.d.l	8,64	b.d.l
MgO	b.d.l	20,10	2,04	b.d.l
CaO	9,90	0,14	0,02	7,41
Na_2O	6,07	0,01	b.d.l	7,34
K_2O	0,11	b.d.l	b.d.l	0,16
Cr_2O_3	b.d.l	0,08	1,25	b.d.l
Total	100,34	99,83	98,06	100,22
Si	2,535	1,935	0,002	2,643
Al	1,458	0,089	1,950	1,358
Ti	-	0,002	-	0,001
Fe^{3+}	-	0,037	0,017	-
Fe^{2+}	-	0,786	0,722	-
Zn	-	-	0,188	-
Mn	-	0,009	0,001	0,001
Mg	-	1,135	0,090	-
Ca	0,475	0,006	0,001	0,353
Na	0,527	0,001	-	0,633
K	0,006	-	-	0,009
Cr	-	-	0,03	-

Table 5. U-Pb data for supracrustal rocks, Mühlig-Hofmannfjella

U-Pb data

		No.	Characteristics[1)]	Weight	U	Th/U[3)]	Pbi[4)]	Pbc[4)]	$^{206}Pb/^{204}Pb$[5)]	$^{207}Pb/^{235}U$[6)]	2 s	$^{206}Pb/^{238}U$[6)]	2 s	rho	$^{207}Pb/^{206}Pb$[6)]	2 s	$^{206}Pb/^{238}U$[6)]	2 s	$^{207}Pb/^{235}U$[6)]	2 s	$^{207}Pb/^{206}Pb$[6)]	2 s
				[ug][2)]	[ppm][2)]		[ppm]	[pg]		[abs]		[abs]			[abs]	[Ma]	[Ma]	[abs]	[Ma]	[abs]	[abs]	[abs]
			AHA240 garnet-sillimanite-cordierite gneiss																			
AHA240	439/18	1	Z sb lp CA [1]	14	181	0,37	0,00	0,9	15638	0,7573	0,0023	0,09279	0,00021	0,79	0,05919	0,00011	572,0	1,2	572,5	1,4	574,1	4,1
AHA240	439/16	2	Z eu tip CA [1]	17	184	0,34	0,00	1,1	16866	0,7538	0,0020	0,09249	0,00019	0,88	0,05911	0,00008	570,2	1,1	570,4	1,1	571,3	2,7
AHA240	439/17	3	Z eu tip CA [1]	16	216	0,30	0,00	1,4	13821	0,7391	0,0019	0,09116	0,00019	0,87	0,05880	0,00008	562,4	1,1	561,9	1,1	559,7	2,8
AHA240	441/S.93	4	M eu eq NA [1]	20	1820	13,80	0,40	10,1	20383	0,7248	0,0017	0,08975	0,00019	0,96	0,05857	0,00004	554,1	1,1	553,5	1,0	551,2	1,6
AHA240	441/S.104	5	M an eq NA [1]	1	10454	4,63	0,49	2,5	22667	0,6933	0,0017	0,08655	0,00018	0,95	0,05810	0,00005	535,1	1,1	534,8	1,0	533,5	1,7
			AHA241 garnet-biotite gneiss																			
AHA241	439/20	6	Z eu lp-tip CA [1]	6	418	0,12	0,00	1,7	12898	1,3126	0,0034	0,13730	0,00029	0,90	0,06934	0,00008	829,4	1,7	851,3	1,5	908,8	2,3
AHA241	439/19	7	Z eu lp-tip flat CA	73	220	0,39	0,00	1,3	70148	0,7526	0,0018	0,09243	0,00019	0,96	0,05905	0,00004	569,9	1,1	569,7	1,0	569,1	1,5
AHA241	439/21	8	Z sb lp-tip CA [1]	35	314	0,26	0,00	1,4	46849	0,7493	0,0019	0,09211	0,00020	0,95	0,05900	0,00005	568,0	1,2	567,8	1,1	567,0	1,8
AHA241	441/S.39	9	M an eq NA [1]	5	3959	18,91	1,09	7,5	15994	0,7910	0,0020	0,09612	0,00021	0,96	0,05968	0,00005	591,6	1,2	591,7	1,1	592,2	1,6
AHA241	441/S.44	10	M an eq NA [1]	1	4495	39,43	2,34	4,4	5627	0,6969	0,0019	0,08685	0,00019	0,87	0,05820	0,00008	536,9	1,1	537,0	1,2	537,2	3,0
			AHA242 garnet-sillimanite-cordierite gneiss																			
AHA242	439/23	11	Z eu lp-tip CA [1]	3	525	0,25	0,00	0,7	12491	0,7498	0,0020	0,09191	0,00018	0,83	0,05917	0,00009	566,8	1,1	568,1	1,2	573,2	3,2
AHA242	439/22	12	Z eu sp CA [1]	15	288	0,24	0,00	1,0	24961	0,7483	0,0019	0,09182	0,00019	0,91	0,05911	0,00006	566,3	1,1	567,3	1,1	571,1	2,3
AHA242	439/24	13	Z eu lp CA [1]	22	199	0,11	0,00	1,7	15113	0,7470	0,0019	0,09174	0,00019	0,90	0,05905	0,00007	565,8	1,1	566,5	1,1	568,9	2,4
AHA242	441/S.36	14	M an eq NA [1]	15	4245	9,45	0,43	8,4	46775	0,8172	0,0021	0,09858	0,00022	0,97	0,06012	0,00004	606,1	1,3	606,5	1,1	607,8	1,4
AHA242	441/S.38	15	M an NA [1]	5	2428	10,30	0,85	6,3	10355	0,6788	0,0016	0,08510	0,00018	0,95	0,05785	0,00005	526,5	1,0	526,1	1,0	524,2	1,7

1) Z = zircon; M = monazite; eu = euhedral; sb = subhedral; an = anhedral; lp = long prisamatic; eq = equant; CA = chemically abraded; NA = non-abraded; [20] = number of grains in fraction

2,4) weight and concentrations are known to better than 10%, except for those near and below the ca. 1 ug limit of resolution of the balance

3) Th/U model ratio inferred from 208/206 ratio and age of sample

4) Pbi = initial common Pb; Pbc = total common Pb in sample (initial + blank)

5) raw data corrected for fractionation

6) corrected for fractionation, spike, blank and initial common Pb; error calculated by propagating the main sources of uncertainty.

Table 6. Results from «Average P» calculation using Thermocalc (Holland and Powell, 1988).

Sample	Assemblage	Av P (kbar)	SdP (kbar)
AHA245	Grt+Sil+Pl Kfs Bt	7.8	1.7
AHA244	Grt+Opx+Pl+Bt	7.7	1.3

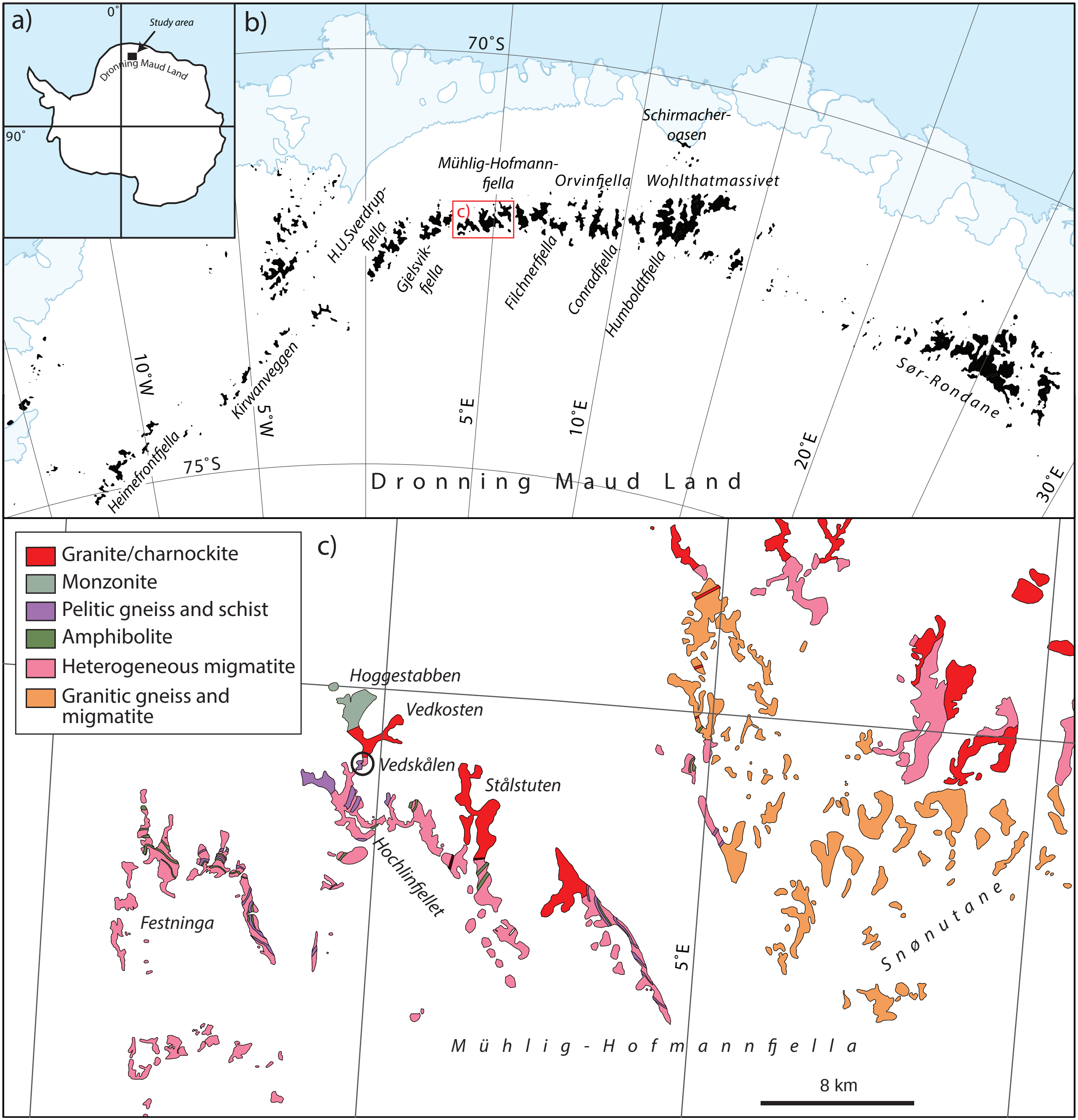
a)
Study area
Dronning Maud Land
0°
90°
b)
70°S
75°S
Schirmacher-oasen
Mühlig-Hofmann-fjella
Orvinfjella
Wohlthatmassivet
c)
H.U.Sverdrup-fjella
Gjelsvik-fjella
Filchnerfjella
Conradfjella
Humboldtfjella
Kirwanveggen
Heimefrontfjella
Sør-Rondane
10°W
5°W
5°E
10°E
20°E
30°E
Dronning Maud Land
c)
Granite/charnockite
Monzonite
Pelitic gneiss and schist
Amphibolite
Heterogeneous migmatite
Granitic gneiss and migmatite
Hoggestabben
Vedkosten
Vedskålen
Stålstuten
Hochlinfjellet
Festninga
Snønutane
5°E
Mühlig-Hofmannfjella
8 km

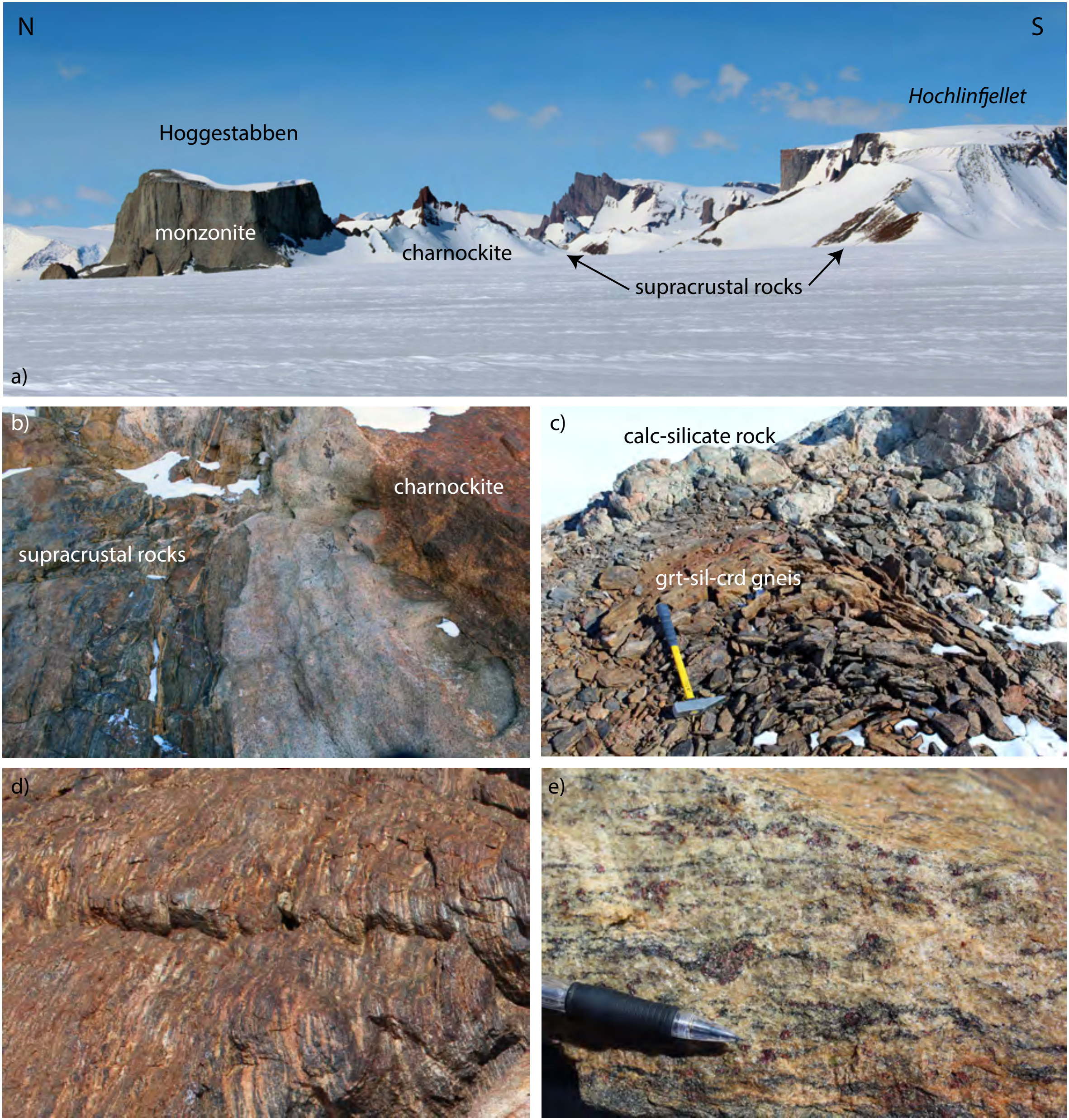
N
S
Hoggestabben
Hochlinfjellet
monzonite
charnockite
supracrustal rocks
a)
b)
charnockite
supracrustal rocks
c)
calc-silicate rock
grt-sil-crd gneis
d)
e)

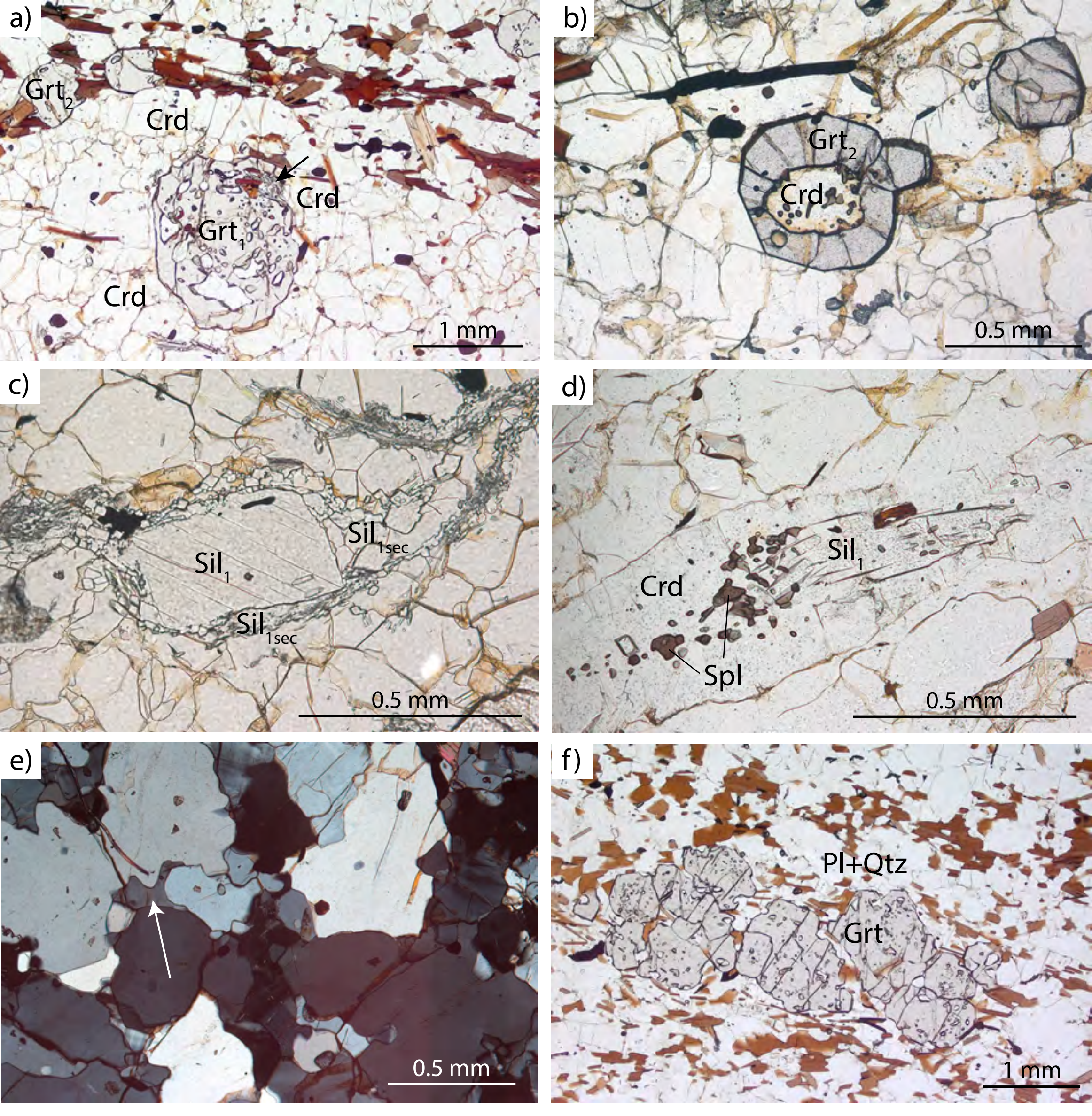
a)
Grt2
Crd
Crd
Grt1
Crd
1 mm
b)
Grt2
Crd
0.5 mm
c)
Sil1sec
Sil1
Sil1sec
0.5 mm
d)
Sil1
Crd
Spl
0.5 mm
e)
0.5 mm
f)
Pl+Qtz
Grt
1 mm

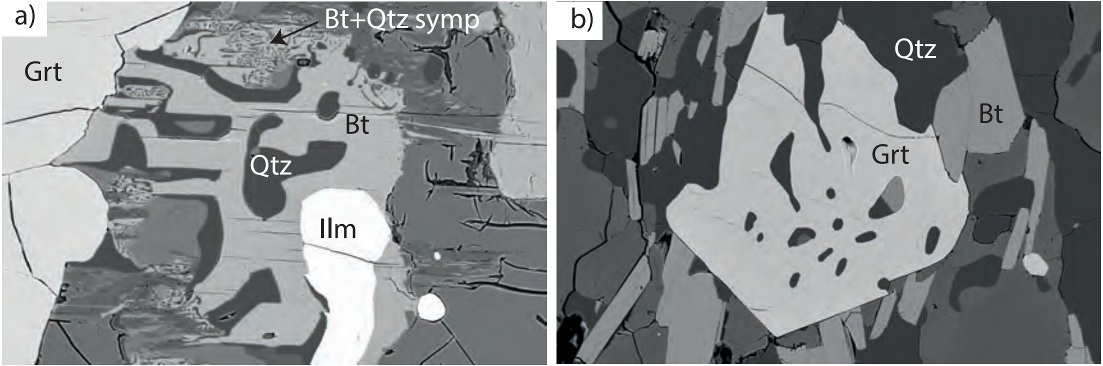

a)
Bt+Qtz symp
Grt
Bt
Qtz
Ilm
b)
Qtz
Bt
Grt

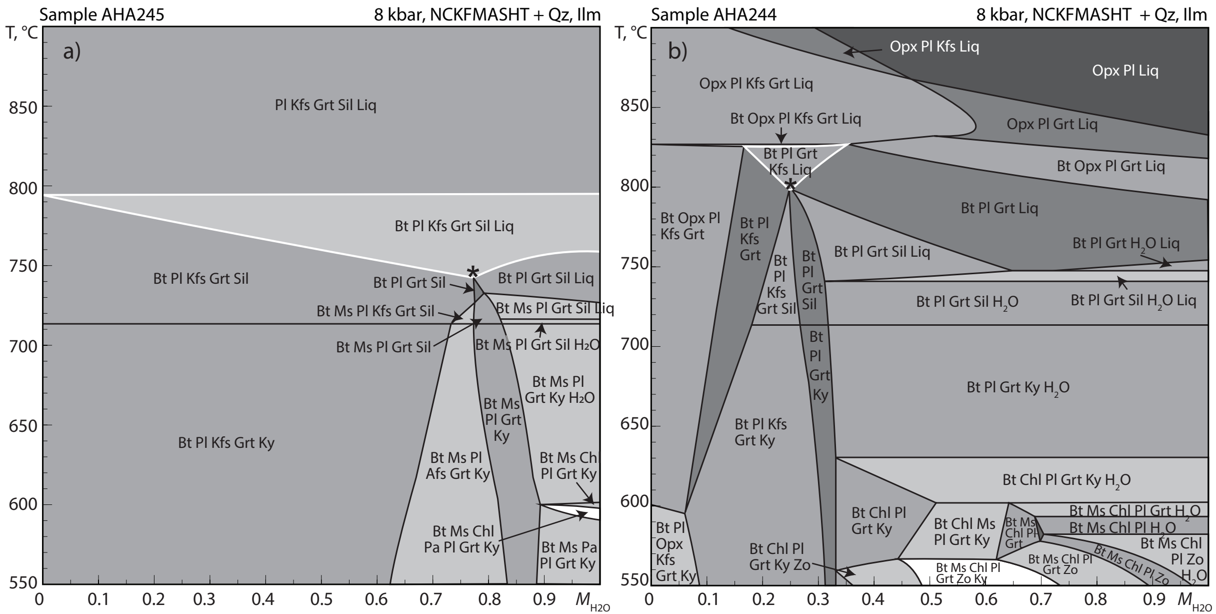

Sample AHA245
8 kbar, NCKFMASHT + Qz, Ilm
a)
T, °C
850
800
750
700
650
600
550
0
0.1
0.2
0.3
0.4
0.5
0.6
0.7
0.8
0.9
M_{H2O}
Pl Kfs Grt Sil Liq
Bt Pl Kfs Grt Sil Liq
Bt Pl Kfs Grt Sil
Bt Pl Grt Sil
Bt Pl Grt Sil Liq
Bt Ms Pl Kfs Grt Sil
Bt Ms Pl Grt Sil Liq
Bt Ms Pl Grt Sil
Bt Ms Pl Grt Sil H2O
Bt Ms Pl Grt Ky H2O
Bt Ms Pl Grt Ky
Bt Pl Kfs Grt Ky
Bt Ms Pl Afs Grt Ky
Bt Ms Chl Pl Grt Ky
Bt Ms Chl Pa Pl Grt Ky
Bt Ms Pa Pl Grt Ky
Sample AHA244
8 kbar, NCKFMASHT + Qz, Ilm
b)
T, °C
Opx Pl Kfs Liq
Opx Pl Liq
Opx Pl Kfs Grt Liq
Bt Opx Pl Kfs Grt Liq
Opx Pl Grt Liq
Bt Pl Grt Kfs Liq
Bt Opx Pl Grt Liq
Bt Pl Grt Liq
Bt Opx Pl Kfs Grt
Bt Pl Kfs Grt
Bt Pl Kfs Grt Sil
Bt Pl Grt Sil
Bt Pl Grt Sil Liq
Bt Pl Grt H_2O Liq
Bt Pl Grt Sil H_2O
Bt Pl Grt Sil H_2O Liq
Bt Pl Grt Ky
Bt Pl Grt Ky H_2O
Bt Pl Kfs Grt Ky
Bt Chl Pl Grt Ky H_2O
Bt Chl Pl Grt Ky
Bt Chl Ms Pl Grt Ky
Bt Ms Chl Pl Grt
Bt Ms Chl Pl Grt H_2O
Bt Ms Chl Pl H_2O
Bt Ms Chl Pl Zo H_2O
Bt Pl Opx Kfs Grt Ky
Bt Chl Pl Grt Ky Zo
Bt Ms Chl Pl Grt Zo Ky
Bt Ms Chl Pl Grt Zo
Bt Ms Chl Pl Zo

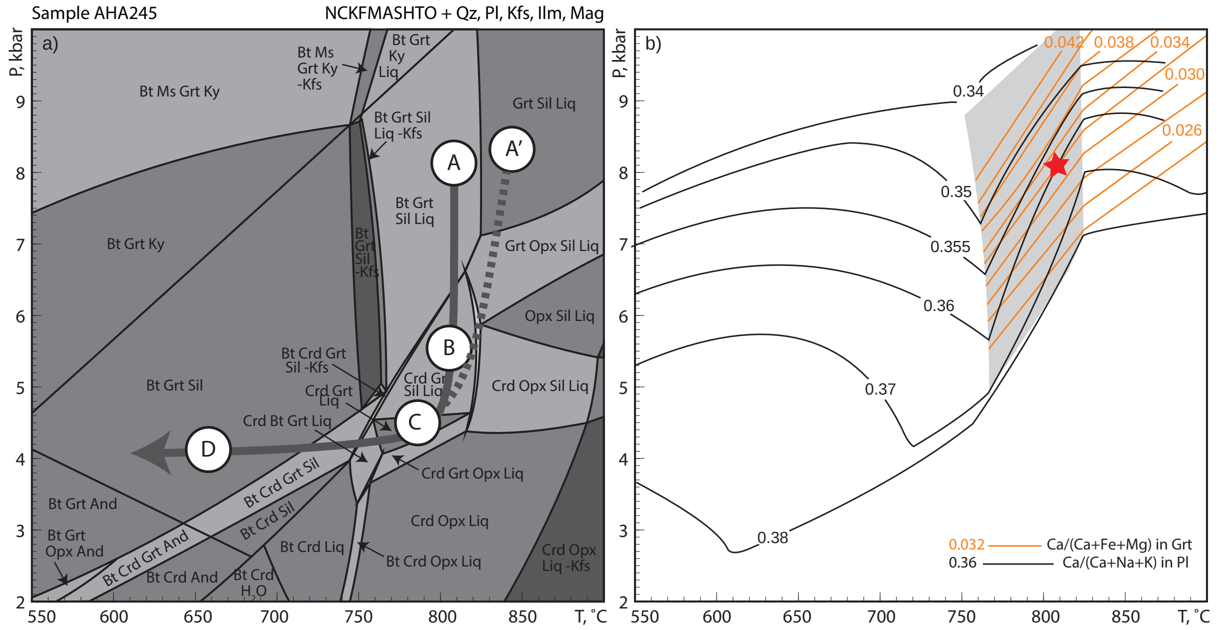

Sample AHA245
NCKFMASHTO + Qz, Pl, Kfs, Ilm, Mag
a)
b)
P, kbar
T, °C
Bt Ms Grt Ky
Bt Ms Grt Ky -Kfs
Bt Grt Ky Liq
Bt Grt Sil Liq -Kfs
Grt Sil Liq
Bt Grt Ky
Bt Grt Sil -Kfs
Bt Grt Sil Liq
Grt Opx Sil Liq
Opx Sil Liq
Crd Opx Sil Liq
Bt Grt Sil
Bt Crd Grt Sil -Kfs
Crd Grt Liq
Crd Grt Sil Liq
Crd Bt Grt Liq
Crd Grt Opx Liq
Bt Crd Grt Sil
Bt Crd Sil
Bt Grt And
Bt Grt Opx And
Bt Crd Grt And
Bt Crd And
Bt Crd H2O
Bt Crd Liq
Bt Crd Opx Liq
Crd Opx Liq
Crd Opx Liq -Kfs
A
A′
B
C
D
0.34
0.35
0.355
0.36
0.37
0.38
0.042
0.038
0.034
0.030
0.026
0.032 Ca/(Ca+Fe+Mg) in Grt
0.36 Ca/(Ca+Na+K) in Pl

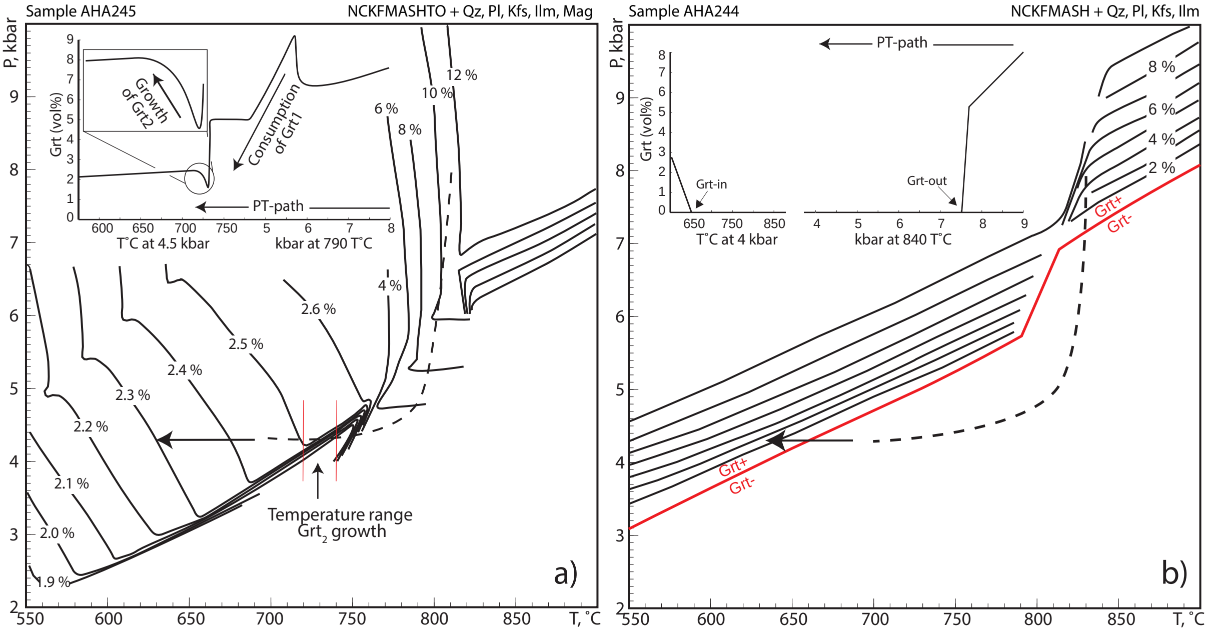

Sample AHA245
NCKFMASHTO + Qz, Pl, Kfs, Ilm, Mag
P, kbar
Grt (vol%)
Growth of Grt2
Consumption of Grt1
PT-path
T˚C at 4.5 kbar
kbar at 790 T˚C
12 %
10 %
6 %
8 %
4 %
2.6 %
2.5 %
2.4 %
2.3 %
2.2 %
2.1 %
2.0 %
1.9 %
Temperature range Grt2 growth
a)
T, ˚C
Sample AHA244
NCKFMASH + Qz, Pl, Kfs, Ilm
P, kbar
PT-path
Grt (vol%)
Grt-in
Grt-out
T˚C at 4 kbar
kbar at 840 T˚C
8 %
6 %
4 %
2 %
Grt+
Grt-
b)
T, ˚C

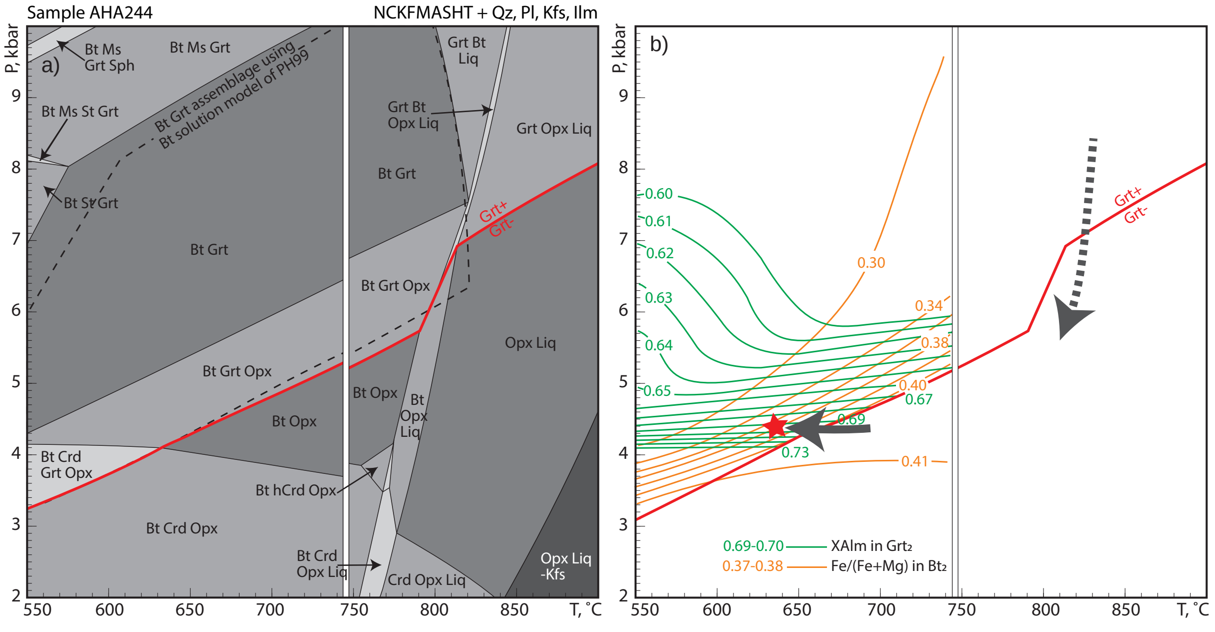
Sample AHA244
NCKFMASHT + Qz, Pl, Kfs, Ilm
P, kbar
a)
Bt Ms Grt Sph
Bt Ms Grt
Bt Ms St Grt
Bt St Grt
Bt Grt assemblage using Bt solution model of PH99
Bt Grt
Bt Grt Opx
Bt Opx
Bt Crd Grt Opx
Bt hCrd Opx
Bt Crd Opx
Bt Crd Opx Liq
Grt Bt Liq
Grt Bt Opx Liq
Grt Opx Liq
Grt+
Grt-
Bt Opx Liq
Opx Liq
Crd Opx Liq
Opx Liq -Kfs
T, °C
b)
0.60
0.61
0.62
0.63
0.64
0.65
0.67
0.69
0.73
0.30
0.34
0.38
0.40
0.41
0.69-0.70 XAlm in Grt₂
0.37-0.38 Fe/(Fe+Mg) in Bt₂
2
3
4
5
6
7
8
9
550
600
650
700
750
800
850

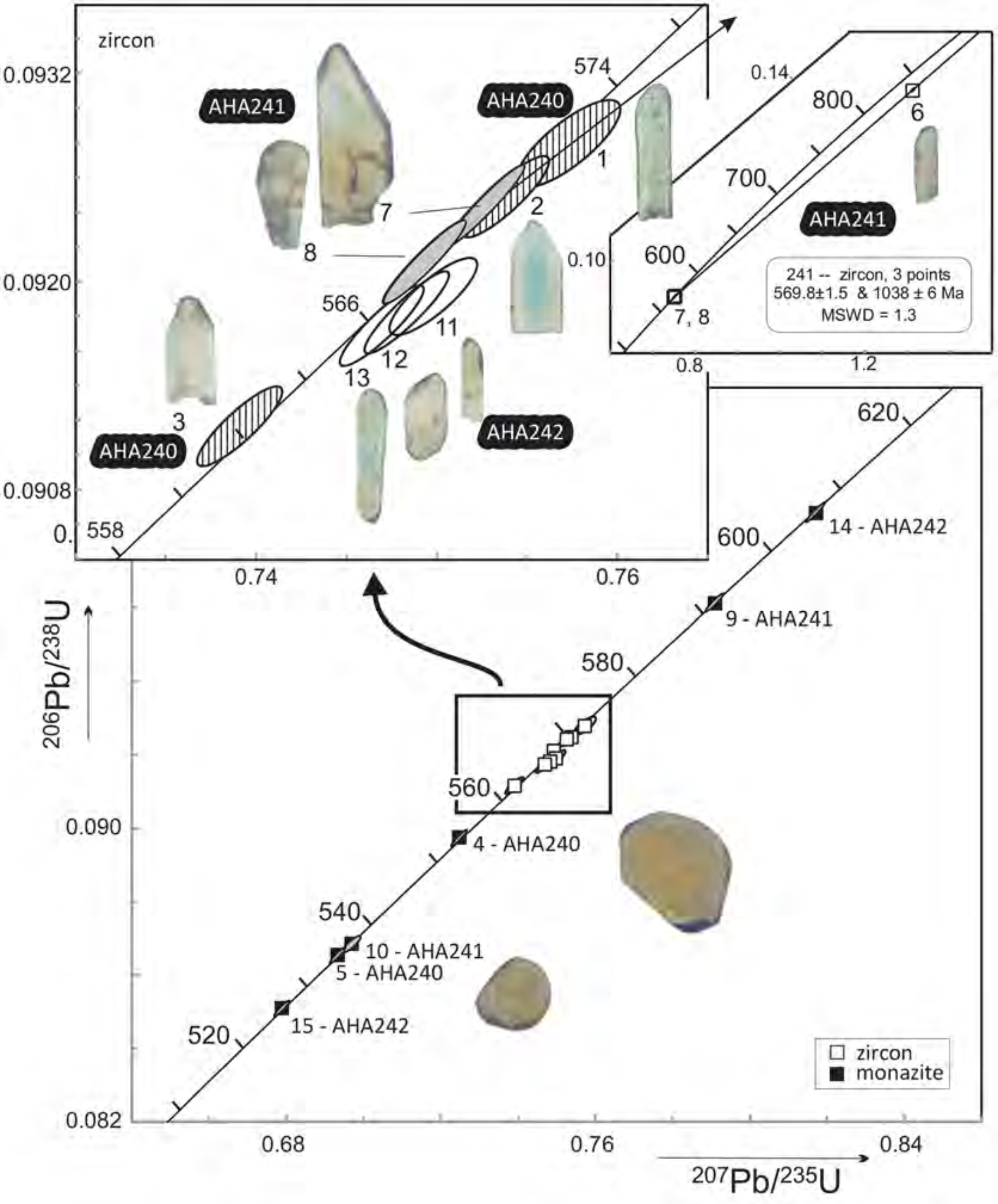

zircon
AHA241
AHA240
AHA242
574
566
558
0.0932
0.0920
0.0908
0.74
0.76
0.10
0.14
800
700
600
6
7, 8
0.8
1.2
241 -- zircon, 3 points
569.8±1.5 & 1038 ± 6 Ma
MSWD = 1.3
620
600
580
560
540
520
14 - AHA242
9 - AHA241
4 - AHA240
10 - AHA241
5 - AHA240
15 - AHA242
0.090
0.082
0.68
0.76
0.84
zircon
monazite
$^{206}Pb/^{238}U$
$^{207}Pb/^{235}U$

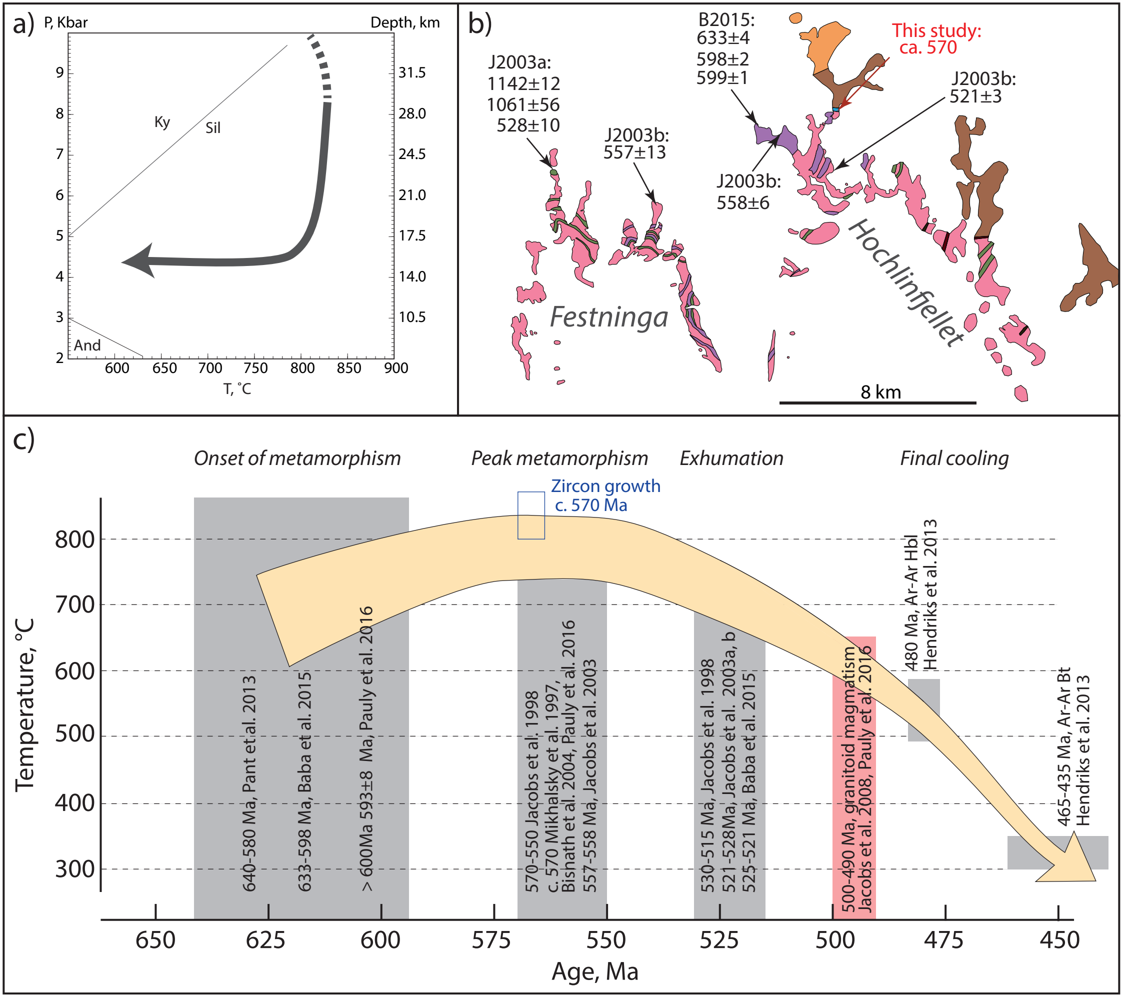
a)
P, Kbar
Depth, km
Ky
Sil
And
T, °C
b)
B2015:
633±4
598±2
599±1
This study:
ca. 570
J2003a:
1142±12
1061±56
528±10
J2003b:
557±13
J2003b:
521±3
J2003b:
558±6
Festninga
Hochlinfjellet
8 km
c)
Onset of metamorphism
Peak metamorphism
Exhumation
Final cooling
Zircon growth
c. 570 Ma
Temperature, °C
Age, Ma
640-580 Ma, Pant et al. 2013
633-598 Ma, Baba et al. 2015
> 600Ma 593±8 Ma, Pauly et al. 2016
570-550 Jacobs et al. 1998
c. 570 Mikhalsky et al. 1997,
Bisnath et al. 2004, Pauly et al. 2016
557-558 Ma, Jacobs et al. 2003
530-515 Ma, Jacobs et al. 1998
521-528Ma, Jacobs et al. 2003a, b
525-521 Ma, Baba et al. 2015
500-490 Ma, granitoid magmatism
Jacobs et al. 2008, Pauly et al. 2016
480 Ma, Ar-Ar Hbl
Hendriks et al. 2013
465-435 Ma, Ar-Ar Bt
Hendriks et al. 2013